
# STUDIES ON PREPARATION AND PROPERTIES OF NANOPHASE METAL OXIDES

**Tarja Turkki**

Doctoral Thesis

---

**Stockholm**
**1999**

**Department of Materials Science**
**Materials Chemistry**
**Royal Institute of Technology**
**S-100 44 Stockholm, Sweden**

Department of Materials Science
Materials Chemistry Division
Royal Institute of Technology
SE-100 44 Stockholm
Sweden

# STUDIES ON PREPARATION AND PROPERTIES OF NANOPHASE METAL OXIDES

**Tarja Turkki**

AKADEMISK AVHANDLING
Som med tillstånd av Kungliga Tekniska Högskolan framlägges till offentlig granskning för avläggande av teknologie doktorsexamen i materialkemi, fredagen den 28 maj 1999, kl. 13.00 i kollegiesalen, KTH, Valhallavägen 79 Stockholm. Fakultetsopponenten är Prof. Horst Hahn, Darmstadt University of Technology, Darmstadt, Germany. Avhandlingen försvaras på engelska.

**Cover Figures**

The SEM micrograph on the right side shows the web-like structure of cerium-zirconium oxide agglomerates prepared using the laser vaporization technique. The photo on the left shows the blue photoluminescence of silica nanoparticles prepared by the same synthesis technique.

*Dedicated to my family*

Learn as though you would never be able to master it;
Hold it as though you would be in fear of losing it.

Confucious

**ABSTRACT**

This thesis is about science on an atomic scale - an interdisciplinary approach to nanoparticles. Studies of the preparation of nanoparticles using both physical and chemical methods are presented. Understanding and controlling factors for particle growth during synthesis are the keys to successful fabrication of materials with tailored properties. The size effects on electronic, magnetic, optical, as well as oxygen storage and catalytic properties have been investigated. The relationship between the structure and physical properties has been examined. The erudition of the fundamentals and the control of the synthesis enables the tailoring of new materials on the atomic scale.

The preparation of nanoparticles using a new technique based on laser evaporation under reactive atmosphere in an upward thermal diffusion cloud chamber was attempted. Unlike other laser evaporation - gas condensation techniques, high vacuum was not needed and atmospheric pressure sufficed. Particles below 10 nm in diameter were successfully prepared without any necking, despite the high pressure. No further treatments like post-oxidation or carburization were needed. It was possible to prepare many different materials: metals, oxides, carbides and nitrides. "New" materials like molybdenum carbide $(MoC_4)_n$ n=1-4 series have been made on a macroscopic scale. Molybdenum was found to catalyze the formation of fullerenes, especially the higher ones, as well as the polymerization of ethylene.

Silicon and iron oxides were synthesized using laser vaporization. Silicon oxide nanoparticles evince photoluminescence. The oxygen-deficient structure of silica gives rise to this phenomenon. The magnetic behavior of iron oxides can be explained in terms of superparamagnetism. The oxidation state of iron oxides could be controlled by the partial pressure of oxygen in the preparation chamber.

Chemical methods were applied for synthesis of nanophase metal oxides. The particle growth and agglomeration of doped cerium oxalates precipitated using the coprecipitation method was studied. Agglomeration was found to be diffusion controlled and proceeded through the cluster-cluster collision mechanism. Optimization of particle morphology by controlling the surfactant selection, pH, dilution and counter ions was performed. DLVO theory was used to explain the particle growth.

The structure, oxygen storage capacity and surface chemistry of cerium-zirconium oxides prepared by laser vaporization and coprecipitation methods were compared. The reducibility of cerium oxide in laser evaporated samples was significantly enhanced and activated at much lower temperatures and this was attributed to the reduction of surface hydroxyl groups. Coprecipitated samples had the highest carbon contamination, which was possibly due to undecomposed carbonates or surface charges that favored carbon dioxide absorption.

The synthesis of doped ceria applying different precipitation sequences was studied and the catalytic activity was compared to a commercial catalyst. Calcium doping increases the oxygen storage capacity remarkably in rhodium catalysts. The lambda window was equal to that obtained for the reference sample despite the lower surface area.

Studies of the catalytic activity of doped cerium oxides with and without precious metals were carried out. High catalytic activity was obtained for manganese and neodymium-zirconium doped samples. Good thermal stability was observed for neodymium-zirconium doped ceria. The light-off temperature of doped cerium oxide catalysts towards CO oxidation was a function of particle size. The surface area on the other hand was found to be related to the electronegativity of the dopant. The heat of formation of the oxides seemed to be directly related to the heat of adsorption of propene and a minimum light-off temperature was found. The catalytic activity of palladium-impregnated ceria samples was a function of the acidity of the cerium oxide support.

***Keywords:*** *nanoparticles, laser vaporization, coprecipitation, $SiO_2$, iron oxide, $CeO_2$, doping, photoluminescence, superparamagnetism, surface chemistry, oxygen storage capacity, catalytic activity, modeling*

## LIST OF PAPERS

This thesis is based on following publications.

**Paper I** "Synthesis and Photoluminescence of Web-like Agglomeration of Silica Nanoparticles"
M. S. El-Shall, S. Li, **T. Turkki**, D. Graiver, U. Pernisz, and M. I. Baraton,
*J. Phys. Chem*. **99**, 17805-17809 (1995).

**Paper II** "Magnetism of Nanophase Iron Particles Laser Evaporated in a Controlled Oxygen Atmosphere",
**T. Turkki**, B. J. Jönsson, V. Ström, H. Medelius, M. S. El-Shall and K. V. Rao,
*J. Korean Magn. Soc*. **5** (Proceedings for 3rd International Symp. on Physics of Magn. Materials), 745-8 (1995).

**Paper III** "Oxidation States and Magnetism of Fe-Nanoparticles Prepared by a Laser Evaporation Technique"
B. J. Jönsson, **T. Turkki**, V. Ström, K. V. Rao and M. S. El-Shall,
*J. Appl. Phys*. **79**, 5063-5065 (1996).

**Paper IV** "The Reduction of $Co^{2+}$ by Polyalcohols in the Presence of WC Surfaces Studied by XPS"
G. Eriksson, H. Siegbahn, S. Andersson, **T. Turkki** and M. Muhammed,
*Materials Research Bulletin* **32**, 491-499, (1997).

**Paper V** "Characterisation of Mixed Nanophase Cerium-Zirconium Oxides Prepared Using Different Techniques"
**Tarja Turkki,** Mamoun Muhammed, Michel Trudeau and M. Samy El-Shall,
*manuscript.*

**Paper VI** "Synthesis and Characterisation of Nanosized Cerium-Zirconium-Calcium Oxides and Their Application in Three Way Catalysts"
Sara Hjelm, **Tarja Turkki**, Mamoun Muhammed and Lothar Mussmann,
*manuscript.*

**Paper VII** "Origin of Catalytic Activity of Doped Cerium Oxide Based Catalysts"
**Tarja Turkki,** Stephane Romero and Mamoun Muhammed, *manuscript.*

**Paper VIII** "Synthesis of Doped Cerium Oxides by Coprecipitation"
**Tarja Turkki** and Mamoun Muhammed, *manuscript*.

**CONTENTS**

## LIST OF ACRONYMS

| | |
|---|---|
| AC | Alternating current |
| A/F | Air to fuel ratio |
| BET | Brunauer, Emmit, Teller |
| DC | Direct current |
| EDX | Energy dispersive scattering |
| EL | Electroluminescence or electroluminescent |
| ESCA | Electron spectroscopy for chemical analysis |
| DLVO | Derjaguin, Landau, Vervey, Overbeck theory |
| FC | Field cooled |
| FTIR | Fourier transform infrared spectroscopy |
| HC | Hydrocarbon |
| HPLC | High performance liquid chromatography |
| IR | Infrared |
| LUMO | Lowest unoccupied molecular orbital |
| MPL | Emission photoluminescence |
| $M_S$ | Saturation magnetisation |
| NDIR | Non dispersive infrared spectroscopy |
| OSC | Oxygen storage capacity |
| PL | Photoluminescence |
| SEM | Scanning electron microscopy |
| STM | Scanning tunneling microscopy |
| SQUID | Superconducting quantum interference device |
| $T_B$ | Blocking temperature |
| $T_c$ | Critical temperature for superconductors |
| TCD | Thermal conductivity detector |
| TEM | Transmission electron microscopy |
| TPD | Temperature programmed desorption |
| TPR | Temperature programmed reduction |
| UV/VIS | Ultraviolet-visible |
| XPL | Excitation photoluminescence |
| XPS | X-ray photoelectron spectroscopy |
| XRD | X-ray diffraction |
| ZFC | Zero field cooled |
| YAG | Yttrium aluminium iron garnet |

## 1. INTRODUCTION

Particles confined in size to less than about 100 nm are referred to as nanoparticles. These can consist of a few up to tens of thousands of atoms. Significant atom fractions are associated with interfacial environments giving rise to change in various properties, since atoms can be stabilized to metastable states having coordination numbers lower than in the corresponding bulk. [1]

Clusters on a nanometer scale can be produced by means of either physical or chemical processes. They may be assembled into nanophase materials, which can be studied by a variety of conventional experimental methods. Ultrafine grain sizes and the rather large number of grain boundaries dominate the structure of nanophase materials. The study of the chemistry and physics of clusters enables us to understand the evolution of basic properties from the atomic to the bulk states of matter.

The history of nanoparticles is quite long. The first nanoparticle-based technology, which is heterogeneous catalysis, was developed in the early nineteenth century. Photography, using silver halide nanoparticles, was developed shortly after. Nevertheless, the major developments within nanoscience have taken place during the last two decades. Today the development of magnetic data storage, microelectronics and chemical sensors has given rise to a multi-million dollar industry in order to obtain improved properties of nanoparticles. [2]

Control of the size and morphology of the phase domains or grains is thus of primary importance in the synthesis of nanostructured materials. Chemical control of the phases and the cleanliness of the interfaces between phases and grains must also be controlled. The surface of nanoparticles is structurally very heterogeneous and may be represented by the model in Fig. 1.

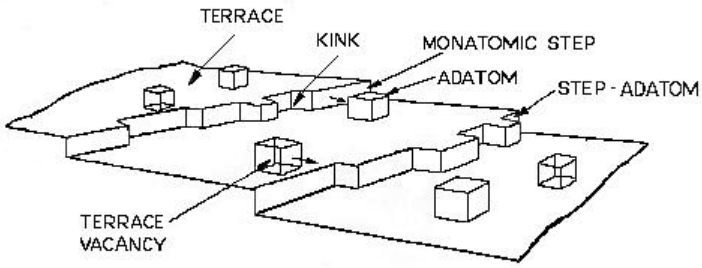


Fig. 1. Model of heterogeneous solid surface of a nanoparticle having different surface sites defined by the number of the nearest neighbors. [2]

There are atoms in terraces surrounded by the largest possible number of nearest neighbors. There are surface irregularities, steps and kinks, in which atoms have fewer nearest neighbors. The relative number of atoms in the different sites depends on the surface preparation (i.e. particle size, method of precipitation or condensation and reduction). However, under most reaction conditions equilibrium is obtained between the different sites due to rapid diffusion. [2] Nanophase materials have a large surface area due to small particle size combined with the occurrence of pores between grains and between agglomerates. The crystallite size, grain boundary structure, and microporosity of nanocrystalline systems may be tailored through synthesis, cluster-consolidation, and heat treatments. The selection of the

system and method of its synthesis can also generate controlled bulk structural defects, such as oxygen deficiency.

Nanoparticles have interesting properties due to their small size, hence a high surface to volume ratio. For example, electronic, so-called quantum-size effects caused by spatial confinement of delocalized valence electrons are dependent on the particle size. The surface to volume ratio is a very important parameter, which becomes more important as the size of the particle is decreased to the nanometer regime. A wide range of materials, such as metals, ceramics and composites, in crystalline, quasi-crystalline, or amorphous phases have been synthesized as nanosized materials. In such materials, a large fraction of atoms occupy the grain boundaries and interfaces. Large surface area gives higher reactivity and diffusion properties which have been utilized in catalysts and solid electrolytes. Thus novel material properties may result from surface 'defects' because interface atomic arrangements constitute significant volume fractions of the material. Vacancies have been attributed to be the source of activity of oxide materials e.g. in redox reactions. Moreover, the transport properties of ionic conductors originate from defects in the crystal lattice. In short, we now have new possibilities to tailor the physical and chemical properties of materials by controlling the size of the particles, by maintaining the surface clean or by selective interfacial doping. [1,3,4] Products with superior performance have been obtained using nano materials. New processing techniques need to be developed for the nanomaterials, which will enable improvements in the properties the final products.

An important aspect in nanoscience is to have reliable surface characterization methods. Since most of the interesting phenomena are totally surface controlled, it is of great importance to be able to analyze the surface structure and reactions in order to understand the fundamental phenomena.

**Main objectives of the thesis**

Nanomaterials are defined by a length scale of less than 100 nm, either in one dimension (thin films), two dimensions (nanowires) or in all three dimensions (nanoparticles). This thesis is focused on the three dimensional nanostructured materials. The main objective of this thesis is to demonstrate how material properties can be modified by tailoring properties, either by direct size effects or via modification of the chemical composition of metastable nanophase materials. This thesis consists of three main parts.

In the first part, the preparation of nanoparticles using the laser evaporation technique is addressed. In this part, the aim was to explore the possibilities of this method with regard to materials preparation and control of the chemical composition and particle size. Formation of ‘new’ materials through catalytic reactions of transition metals in the plasma was studied. Interesting properties of nanophase metal oxides like photoluminescence and magnetic properties were investigated.

The second part of the thesis is focused on the use of chemical methods (mainly coprecipitation) for the synthesis of nanoparticles. This includes studies of the particle growth and control of the agglomeration during precipitation. The effect of precipitation procedure on the catalytic properties of calcium and zirconium doped ceria was examined in terms of

the physical properties of the samples. A comparison of the surface chemistry and oxygen storage properties of zirconium doped cerium oxide materials, prepared by chemical and laser vaporization methods was undertaken. The origin of catalytic activity of doped cerium oxide materials was studied and an attempt to establish the structure-property relationship of the observed catalytic activity and properties of the oxide, e.g. surface area, size of vacancy, heat of adsorption and acidity was made.

The third part of the thesis is concerned with a surface study of solid-liquid interfaces and to evaluate the effect of the tungsten carbide surface on the reduction of cobalt. The reaction mechanism of the reduction of cobalt, using polyethylene glycol, was investigated.

## 2. PROPERTIES OF NANOPARTICLES

There are numerous material properties that are affected by decreasing the grain size within the material. This chapter summarizes some of the most important properties of nanophase materials. Catalytic properties have been studied the most. Catalytic, electronic and magnetic properties of nanophase materials have important applications. Also, the transport properties play an important role in technological development. These properties make nanophase materials attractive to study both for fundamental aspects as well as for potential novel applications.

### 2.1 Catalytic Properties

Studies on catalytic properties are predominantly based on single crystal surfaces of metal in vacuum. There is very little information on catalytic processes involving oxides. Catalytic reactions involve the following general surface chemical steps [2]
1. Adsorption of the reactant molecules at surface sites
2. Bond breaking of the adsorbates
3. Rearrangement of the adsorbed reaction intermediates
4. Desorption of the molecules

The influence of decreasing the particle size at different stages in catalysis is discussed in the following sections. Materials become more stepped and rough as the particles become smaller in size. Doping gives rise to anisotropic surfaces.

#### 2.1.1. Particle Size Dependence of Surface Processes

Several surface processes are dependent on the surface structure and particle size. It has been shown that some catalytic reactions are structure insensitive, and only one active surface metal atom is needed. For structure-sensitive reactions several adjacent active surface atoms are needed. Reactions involving C-H bond formation or breaking are usually structure insensitive, while reactions involving C-C bond breaking/formation are usually structure sensitive. For the structure-sensitive reactions particle size and other properties can be of importance. Both catalytic activity and selectivity can be dependent on particle size. [5]

**Adsorption**

All catalytic reactions proceed through adsorption. The adsorbate atoms are trapped at sites where the well depth of the attractive surface potential is higher than the kinetic energy of the atoms. The sticking probability of atoms is defined as the rate of adsorption divided by the rate of collision, and it is higher for more open and rough surfaces than on flat ones. This is due to the higher heat of adsorption at a kink or step edge site.

**Diffusion and desorption**

Diffusion is very fast on catalyst surfaces and requires a much lower activation energy than desorption. Diffusion is anisotropic since diffusion rates parallel to steps are greater than diffusion rates perpendicular to steps. The presence of co-adsorbates influences surface diffusion markedly. Elements that decrease the melting point of the substrate cause an

increase in surface diffusion rates and a decrease in activation energies for diffusion in general.

The desorption of atoms from kink and step sites requires a much higher energy than from flat surfaces. The change of surface from flat to stepped and kinked gives the material a wider range of desorption/adsorption energies.

**Work function**

The work function is the ionization potential required to eject the most loosely bound electrons into vacuum at 0 K. The work function is dependent on both the surface roughness and the particle size of the material. It is easier to ionize metals when step density increases, as shown in Fig. 2.

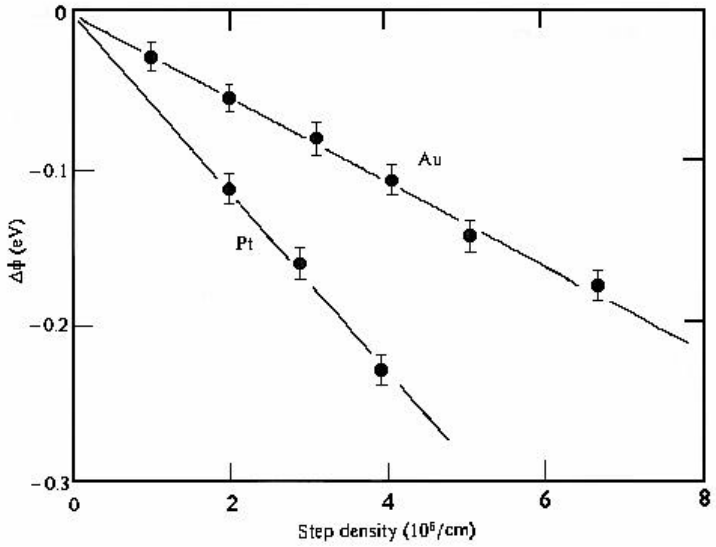


Fig. 2. The work function of stepped gold and platinum surfaces as a function of step density (roughness). [6]

The effect of particle size on the work function is less studied but there is evidence that the ionization potential increases with decreasing particle size (Fig. 3.). It is not yet known whether these changes are due to changes in cluster structure or some other effect.

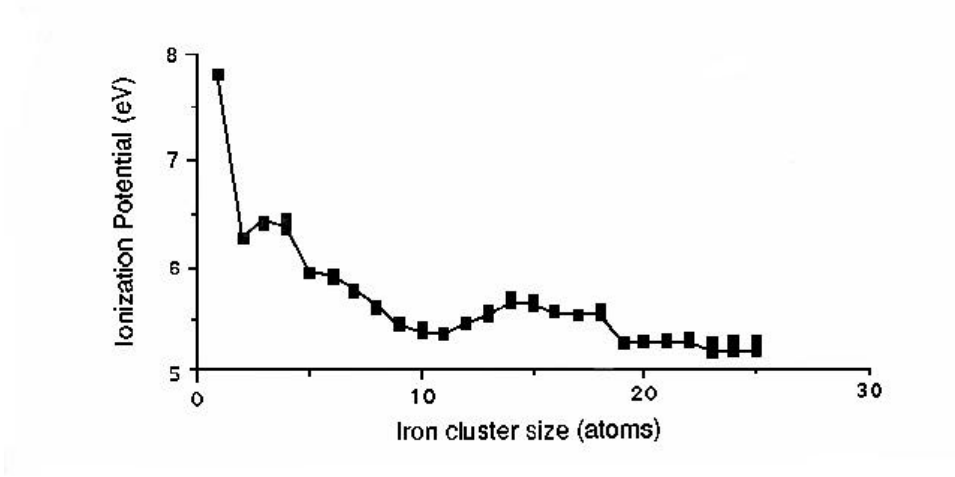


Fig. 3. The ionization potential of iron clusters as a function of cluster size. [6]

**Bond breaking**

Bond breaking of the adsorbate molecules is the main function of catalysts. Bonding of adsorbate to metal generally increases from left to right in the periodic table. The d-electron back bonding depends on the degree of filling of the antibonding states. This means that early transition metals with fewer d-electrons form stronger chemical bonds. The heat of adsorption correlates with the heats of formation of the corresponding oxides and hydrides.

Molecules dissociate on more open and atomically rough surfaces at lower temperatures than on flat, and close-packed surfaces. The heat of adsorption is higher at defect sites on a surface. Defect sites, surface roughness and low packing density of surfaces give rise to higher charge densities near the Fermi level. The work function of these sites is lower and the density of filled electronic states is higher. They are likely to have more adsorbate-induced restructuring. These factors can give rise to enhanced reactivity and bond strength and lead to surface-structure sensitivity of the adsorbate bond. Atomic steps break H-H and C-H bonds efficiently while kinks in the steps are required for additional C-C and C=O bond scissions. [2]

**Charge transfer**

Most of the catalytic reactions involve charge transfer of either electrons or protons. Electron transfer capability is described as a site being able to receive a pair of electrons (Lewis base) or having a free pair of electrons that can be transferred to the adsorbate (Lewis acid). Acidity of metal ions of equal radius increases with increasing charge. The binding energies of the charge-transfer complexes determine the strength of Lewis acidity. Proton transfer requires Broensted sites that can lose (acid) or accept (base) a proton. The acidity of oxides is related to metal-oxygen bond energy. The general rule is that acidity increases as a function of charge on the metal ion.

Acidity of mixed oxides have been studied in the context of Tanabe's model [7]. It is based on two fundamental assumptions;

1) The coordination numbers of the mixed cations are maintained
2) The coordination number of the anion (oxygen) will be that of the major component oxide. There will be charge imbalance due to the rare coordination. Acidity will be increased. Bonds can contract due to impurity contamination [8] and X-O-Y bonds exist.

The acidity of a surface has a large effect on catalytic behavior of an oxide material. Acidity is very important in some catalytic reactions [9], of which the most important is catalytic cracking. In cracking a variety of other processes besides "cutting" of the carbon chains take place. Each of these processes only occurs on sites of the appropriate strength and nature [10].

The initial reactions which form carbonium and carbenium ions require both strong Brønsted and Lewis acid sites. The formation of carbocations is the rate-controlling step in the cracking of alkane. The number of hydroxyl groups together with the crystal structure, surface area, size distribution and porosity determines the rate of production of electron - hole pairs, the surface adsorption and desorption processes and the redox process.

### 2.1.2 Three Way Catalyst

The catalytic converters used in automobiles are called three-way catalysts because they catalyze three reactions, namely: Oxidation of hydrocarbons and carbon monoxide to $CO_2$ and reduction of $NO_x$ to $N_2$. Precious metals (Pt, Pd, Rh) catalyze these reactions. Unfortunately the amount of material to be oxidized (HC and CO) should be stochiometric [14] with the gases to be reduced ($O_2$ and NO) in order for the catalyst to function properly. (Fig. 4)

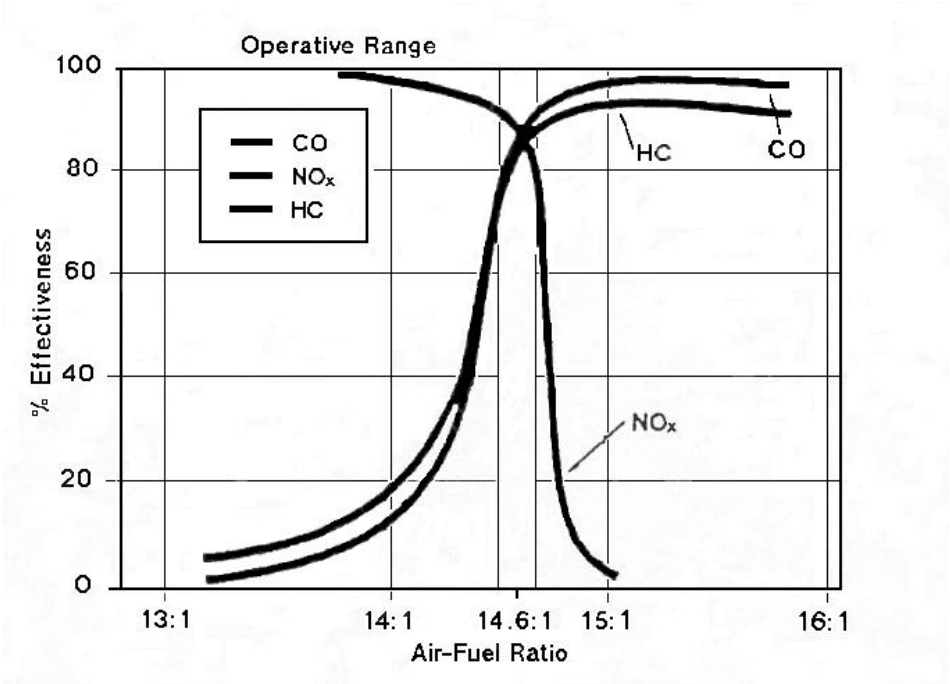


Fig. 4. Conversion of hydrocarbons, CO and NO in a three way catalyst as a function of air to fuel ratio. [14]

The air to fuel ratio ($\lambda$) window is very important and is generally very narrow. In order to widen this window, cerium oxide is added to the support. Cerium oxide works as an oxygen buffer releasing oxygen under reducing atmosphere thus transforming to $Ce_2O_3$. Under oxidizing conditions cerium can be re-oxidized to $CeO_2$.

**Reactions of hydrocarbons, CO and NO**

Oxygen adsorption on metal surfaces is accompanied by an increase in the work function. Weakly adsorbed molecular oxygen is dissociated very fast to partly ionized atomic oxygen. Oxygen adsorption causes some surface reconstruction and it can penetrate beneath the surface layer and cause metal oxidation. [15]

Platinum is the most commonly used catalyst for carbon monoxide oxidation. Carbon monoxide adsorbs on metal sites; either on top or bridge sites [15]. Bridge sites have the highest bond strength and these sites adsorb all CO at low coverage. The top sites become more important at a coverage of about 0.30 and higher. Metals on the left side of the Periodic Table, dissociate CO and atomic species are then adsorbed on hollow sites on the metal [6].

There are two reaction mechanisms occurring on ceria-supported catalysts. In addition to the reaction with noble metals there is another mechanism arising from the combination of rhodium and ceria. Oxygen from ceria reacts with CO from rhodium and the activation energy for this path is lower than the conventional mechanism. This mechanism becomes more important for small metal particles, at high CO pressures and at low temperatures. In CO hydrogenation reactions on supported metal catalysts there is a correlation between the reaction rate enhancement with the oxidation state of the metal of the support oxide as well as the electronegativity (= Lewis acidity) of that metal. CO is bound to a site on the metal/metal oxide support in this reaction via its carbon end to the metal catalyst and via its oxygen end to the Lewis acidic oxide. [16]

NO and CO are very similar molecules, as they both have accessible $2\pi*$ antibonding orbitals. Nevertheless, there is the difference that NO has an electron occupying this orbital whereas CO does not and therefore, NO is easier to dissociate. [17] At low coverage all NO dissociates, while at higher coverage part of NO desorbs when the reaction takes place at room temperature. Rhodium is the best catalyst for reduction of NO to $N_2$ either by carbon monoxide [18] or hydrocarbons [19]. NO dissociation can be written as: $2NO \rightarrow N_2 + 2O$ and the oxygen intermediate reacts readily with for example CO.

Hydrocarbon oxidation requires the breaking of both C-H and C-C bonds. Adsorbed unsaturated hydrocarbons decompose developing hydrogen and leaving the precious metal surface covered with partially dehydrogenated carbon fragments. These carbon species dehydrogenate sequentially over a range of temperature. [6]

**Oxides in three way catalysts**

Oxide materials used in three way catalysts can be divided to two groups. The first group being the very stable oxides like silicon dioxide and aluminum oxide that are stable under the reaction conditions. These oxides are used as catalyst supports to disperse catalyst and give it a high surface to weight ratio. The second group of oxide materials are the transition metal

oxides that can catalyze redox reactions by actively taking part in the reactions through transfer of the lattice oxygen of the oxides. These oxides require a high oxygen vacancy mobility [20,21]. Nanophase materials have a high vacancy concentration combined with a large surface area and high diffusivity which increases the catalytic activity of the oxide materials.

The rate of hydrogenation of polar molecules is greatly enhanced by deposition of transition metal oxides on transition metal catalysts. It is proposed that the highly active sites are formed on the metal/metal oxide interfacial area. These sites are expected to be cationic or anionic vacancies present at the edge of the metal oxide moieties. This interaction is thought to weaken the C=O bond, thus facilitating its cleavage or hydrogenation. The oxidation state of a given oxide is lower during $CO_2$ hydrogenation than CO hydrogenation. This is related to the higher hydrogen concentration on the surface of the catalyst in the former case.

The spillover phenomenon refers to migration of mobile species across two phases. In three way catalysts, oxygen in particular can be transported between the noble metal islands and the oxide support. Ions can move in both directions depending on the ambient atmosphere. Spillover is strongly dependent on the basicity of the oxide phase as well as the size and morphology of the noble metal particles. For cerium oxide O spillover is very fast while hydrogen spillover is totally suppressed. [22]

Studies of the relation between particle morphology and the structure of the metal support interface, and catalytic properties have been performed on several different metal-support systems for different reactions. Vaarkamp et al. [23] found that high temperature aging of Pt/$\gamma$-$Al_2O_3$ changed the Pt particle morphology from three- to two-dimensional, and the particle support interface. Hydrogen in the interface was desorbed. These changes in the structure affected the catalytic, chemisorption and electronic properties. Aging decreased the selectivity of this catalyst for hydrogenolysis of neopentane and methylcyclopentane to methane. At the same time, the activity of the isomerization of neopentane and ring opening of methylcyclopentane increased. On the electronic level, the number of holes in the d-band increased. All these changes in properties are related to the change in structure of the metal-support interface.

## 2.2. ELECTRONIC PROPERTIES

For small particles, the wave functions of electrons and holes are confined to the particle volume. If the particle size becomes comparable to or smaller than the de Broglie wavelength of the charge carriers, the confinement increases the energy required for creating an electron/hole pair. This increase shifts the absorption/luminescence spectra towards shorter wavelengths (so called "blue shift" [4]) as shown in Fig. 5. In direct gap semiconductors, the band gap increases with decreasing particle size, and the excited electronic states become discrete with high oscillator strength. The optical absorption spectrum of $\gamma$-$Fe_2O_3$ is red shifted, which can be explained by the lattice strain in small particles [24]. In a polymer matrix $\gamma$-$Fe_2O_3$ shows optical transparency in the visible range.

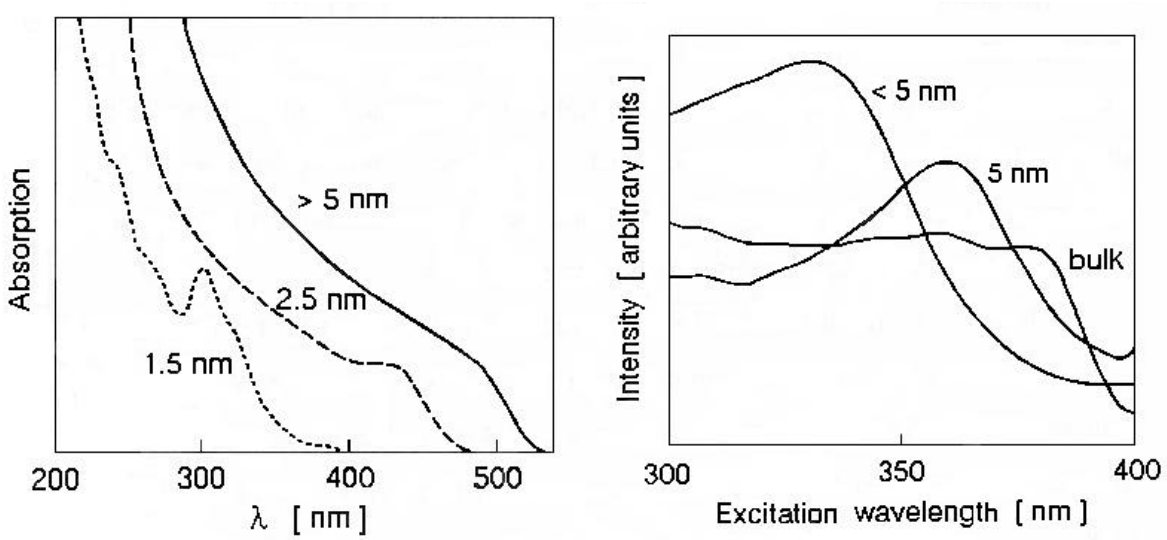


Fig. 5. Absorption spectrum of CdS particles in aqueous solution as a function of particle size (left). Photoluminescence spectra of nanocrystalline ZnO with different crystal sizes in comparison with the bulk material (right). [4]

### 5.1 Indirect Semiconductors

Nanocrystalline Si and porous Si are indirect semiconductors where the absorption involves both a photon and a phonon because the conduction and valence bands are widely separated in k space [25]. Fig. 6 shows the differences in optical absorption and optical transition in direct and indirect gap semiconductors.

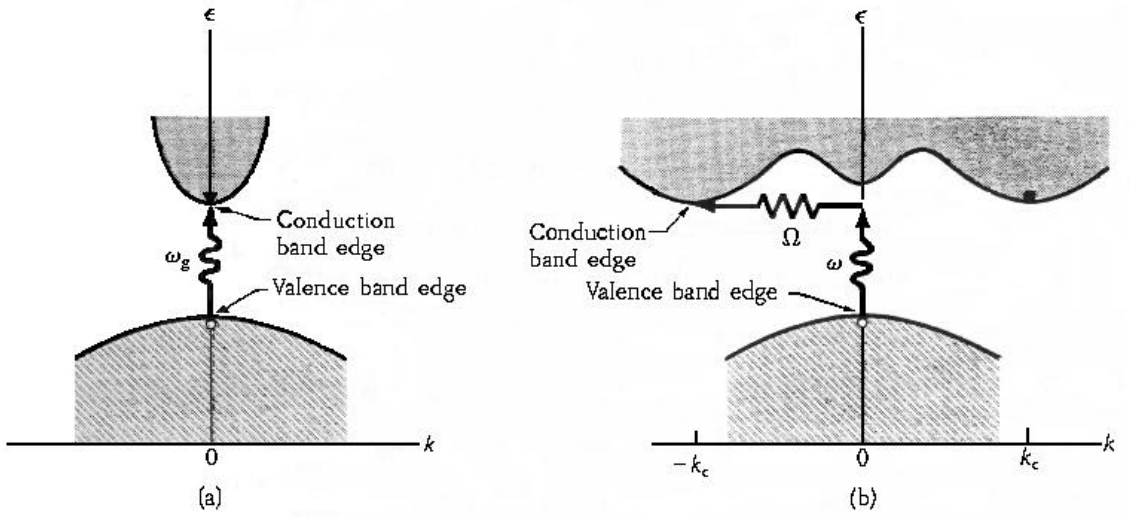


Fig 6. Optical absorption in pure insulators with direct and indirect gaps at absolute zero. [25]

A direct photon transition at the minimum gap can not satisfy the requirement of conservation of energy, because photon wavevectors are negligible at the energy range of interest. But if a phonon of wavevector K and frequency Ω is created in the process, then the excitation can occur.

Several vibronic interactions should increase when wave functions become more compact in nanocrystals. Thus, the vibronic luminescence rate as well as the electronic luminescence rate should increase with decreasing size in nanocrystals. For sizes larger than roughly 15 Å, the vibronic luminescence dominates. Although these nanoparticles have high luminescence yields, the oscillator strengths of nanocrystalline Si and porous Si are not markedly increased with respect to bulk Si [25,27]. In silicon the quantum size effect is primarily kinetic, while in the conventional semiconductors the effect is more spectroscopic [28]. Silicon luminescence increases because spatial confinement keeps the electron and hole superimposed and because surface nonradiative rates are also extremely slow.

### 2.2.2 Photoluminescence of Silicon

Observation of photoluminescence, (PL), in porous silicon [29] generated strong interest, because it opened the door for consideration of silicon as a potential optical material which could be directly integrated into electronic circuits. It is generally recognized that the size of nanophase silicon structures plays a significant role in the luminescence. The shift of the emitted photon energy as the size decreases is usually explained in terms of quantum confinement. Solving the precise mechanism of luminescence has not yet been possible because of the complexity of the modified material. The details of the microstructure, possible existence of several phases in the material, the enormous surface area per unit mass, optical absorption and energy migration are factors which are not yet fully understood.

There are several theories for the mechanism of luminescence involving different physical and chemical factors like the role of surface H [30], the Si dangling bonds [30], involvement of O [31], the near surface electronic states [32], space charge effects [33] and free-carrier recombination [34] in the luminescence process.
Orange-yellow emission of high efficiency (>1%) is generally observed for silicon. Blue photoluminescence has been obtained for oxidized samples [31,35]. Bright visible emission is also observed in electroluminescence.

A comparison of the density of holes due to P-type doping with the size of the nanocrystallites shows that only a few of the nanocrystallites less than 5 nm in diameter will have extrinsic holes available for luminescent recombination. In addition, most theories of porous Si formation postulate the self-termination of the etching process due to the self-limitation in the mobility of holes through the porous Si. By its nature, porous Si does not conduct holes well. PL is allowed because hole - electron pairs are generated in a single nanocrystallite. While PL processes predominate in the region of small nanocrystallites, holes are more available in the larger, more contiguous structures, making EL more favorable. In the region at the interface, with good electrical connectivity to the P-type substrate, the recombination will closely follow the rate of hole and electron transport, as it does for faster EL. [36]

Porous silicon usually shows red-orange electroluminescence but it is possible to produce any of four colors depending on excitation conditions. A reversible spectral shift as large as 270 nm has been obtained for an external bias variation of 0.6 eV [37]. Similar results have been obtained by changing the illumination wavelength used to create holes in the particles and controlling the particle size [38] and different EL spectra with different spectral distributions were obtained.

### 2.2.3 Photoluminescence of Silica

The well known optical absorption band at 5.03 eV (the B band) and luminescence band at 4.3 eV in amorphous $SiO_2$ are due to singlet-to-singlet transitions, while the luminescence band at 2.65 eV is due to triplet to singlet transitions in the silicon related intrinsic defect [39]. This defect occurs both in the bulk and on the surface. In the notation developed for the valence alternation defects in $SiO_2$, this defect may be noted as $Si_2^o$, where 2 stands for coordination and 0 for the net charge. Such defects form a separate class of valence alternation defects, characteristic for amorphous materials having atoms in tetrahedral coordination. The '$B_2$' band is due to a silicon-related defect because it is enhanced in reduced samples and is decreased by oxidation. In the $SiO_2$ glass network Si atoms occupy sites with the highest local symmetry, $T_d$. It is likely that the symmetry will be lower when defects involving this site are formed. Such a model is also consistent with the almost complete similarity between the surface and bulk centers, as well with the weakness in inhomogeneous broadening effects for the bulk centers (good exponential decay of PL). Those effects should be small in this model, because the geometry of the $SiO_4$ tetrahedron is preserved in the $SiO_2$ glass and hence - the distance between the two oxygen atoms, interacting with $Si_2^o$ remains the same.

The PL intensity of oxidized silicon nanoparticles' shows a steep increase from room temperature up to about 120$^o$C and then begins to decrease gradually with rising temperature [40]. When the temperature is reduced below 400$^o$C, the PL intensity increases quite steeply, although it decreases again with decreasing temperature below 200$^o$C. The peak photon energy was found to show a steady decrease with increasing temperature, and remained constant while the temperature decreased. Therefore, the final value of the peak photon energy becomes considerably lower than the initial value. Both the PL intensity and the peak photon energy return to the original values with a long recovery time (10 days or more), indicating that the anomalies are related to structural changes in the material. In fused silica, one emission band appears to identify the luminescent center as the $O_2^-$ molecular ion [41].

## 2.3 MAGNETIC PROPERTIES

### 2.3.1 Magnetism of Multi and Single Domain Particles

A crystal will spontaneously break up into a number of domains in order to reduce the large magnetostatic of single domain particles. Dipolar energy can be reduced by dividing a magnetic specimen into uniformly magnetized domains of macroscopic size, whose magnetization vectors point in widely different directions. Such subdivision is paid for in exchange energy, for the spins near the boundary of a domain will experience unfavorable exchange interactions with the nearby spins in the neighboring domain. Only the spins near the boundaries will have higher exchange energies but the magnetic dipolar energy drops for every spin when domains are formed [42]. When the crystal size is reduced below a critical value $L_c$ of a few hundred Ångströms a single crystal will become a single domain. In the single domain particles (SD) it is not energetically favorable to get magnetization reversed in the particle so no walls are formed.

The extrinsic magnetic properties of particles depend strongly upon their shape and size. This result was obtained when magnetostatic, exchange and domain wall energies were considered. Interactions between particles also affect the critical size. Among magnetic properties coercivity $H_c$ shows a marked size effect. Saturation magnetization on the other hand is not dependent on the particle size. [43]

### 2.3.2 Superparamagnetism

Superparamagnetic particles posses a magnetic moment that may be many orders of magnitude greater than that of a paramagnetic atom $\mu = M_sV$ and, if a field is applied, the field will tend to align the moments of the particles. Thermal energy on the other hand will tend to misalign them. This is just like the normal paramagnetic behavior, just with an exceptionally large magnetic moment. In very small particles random thermal forces are large enough to cause the magnetization direction to reverse spontaneously between the easy directions [44]. The average time between reversals is an exponential function of the ratio of the particle volume to absolute temperature. A particle will spontaneously reverse its magnetization even in the absence of an applied field when the energy barrier to rotation is about 25kT [45]. When the field is turned off the initial magnetization will begin to decrease due to the thermal energy. The rate of decrease is proportional to the magnetization existing at the time and to the Boltzmann factor $e^{KV/kBT}$. Particles that exhibit superparamagnetic behavior have a large saturation magnetization but no remanence or coercivity. Hysteresis will appear and super-paramagnetism disappears, when particles of a certain size are cooled to a particular temperature, or when the particle size, at constant temperature, increases beyond a particular diameter. For superparamagnetic particles magnetization curves measured at different temperatures superimpose when M is plotted as a function of H/T. Since the direction of magnetization in SP particles is changing, the particles cannot be used for magnetic recording. Potential applications of nanoscale magnetic particles are in color imaging, ferro fluids and magnetic refrigeration.

Nano size metallic particles may be so reactive that they undergo surface oxidation [46-49]. Magnetism of these particles can be explained with a core - shell structure, where the core consists of metallic iron and the shell is composed of iron oxides. The magnetic properties depend strongly on particle size and the amount of oxidation. The saturation magnetization is determined from M vs. $1/H^2$ plots by extrapolating the value of magnetization to infinite fields. $M_s$ was found to increase with increasing particle size. The decrease in magnetization with decreasing particle size is related to the higher surface to volume ratio in the smaller particles resulting in a much higher contribution from the surface oxide layer.

The temperature above which superparamagnetic behavior is observed is referred to as the blocking temperature, $T_B$. Below the blocking temperature thermal fluctuations are not sufficient to reverse the magnetization and an irreversible magnetization curve is observed. $T_B$ decreases with decreasing particle size and is sensitive to the chemical composition. Determination of the blocking temperature is easily done in ZFC, FC measurements.

When the measuring time is much shorter than the relaxation time the magnetic moment appears motionless and measurements correspond to static conditions. A time average is detected if the measuring time is much longer than the relaxation time [50]. The blocking temperature is the temperature for which measuring time is equal to the relaxation time.

Blocking temperature depends on the time scale of the measurement so that the blocking temperature is $1/T_B$ is function of ln(f).

The coercivity of the particles is found to depend strongly on particle size [46,47]. $H_c$ decreases as a function of temperature and decreasing particle size makes the difference in coercivity larger by increasing the coercivity at low temperature and dropping to zero at lower temperatures. Larger surface to volume ratio could result in a higher effective anisotropy with large contributions, from the surface and interface anisotropy. In addition to the usual magnetocrystalline and magnetostatic anisotropies, often there are strong influences from the anisotropies due to strains, surface and magnetic interactions coming from the other particles. Experimentally it has been found that K is one or two orders of magnitude larger for Fe, Fe-oxides and Fe-$SiO_2$ in the nanosize particles than in bulk [46,47]. The large effective anisotropy is thought to partly originate from the shell-type particle morphology with strong shell-core interactions and partly from the large surface effects expected in ultrafine particles.

## 2.4. MECHANICAL PROPERTIES

In plastic deformation, grain size reduction can yield improvements in strength and hardness. Grain size reduction increases the strength and hardness, due to new grain boundaries, which act as effective barriers to dislocation motion. However, it may affect other mechanical properties negatively, such as creep rate and ductility. On the other hand, in materials that are conventionally quite strong but very brittle, such as intermetallic compounds and ceramics, enhanced ductility from grain size reduction, through the increased grain boundary sliding, can be considered favorable. [51-54]

### 2.4.1 Hardness

While the hardness of pure metals clearly increases as their grain size is reduced into the nanophase regime (Fig. 7), the results are dependent upon the method used to vary the grain size. Increased hardness with decreased grain size conflicts with the softening of nanophase materials seen in samples annealed to increase their grain size. Intermetallic alloys show initial hardening with decreasing grain size, but at further reduced grain sizes two different cases with either hardening at a reduced slope or softening can be separated. Although hardening in nanophase materials is analogous to Hall-Petch strengthening it is considered to result from different mechanisms. The grain sizes in ultrafine particles are smaller than the critical bowing length for Frank-Read dislocation sources needed to operate at the stresses involved and smaller than the normal spacing between dislocations in a pile-up [1]. The presence of sample porosity, flaws, or contamination from synthesis and processing could influence the available hardness results, as could the nature of the grain boundaries and their state of relaxation.

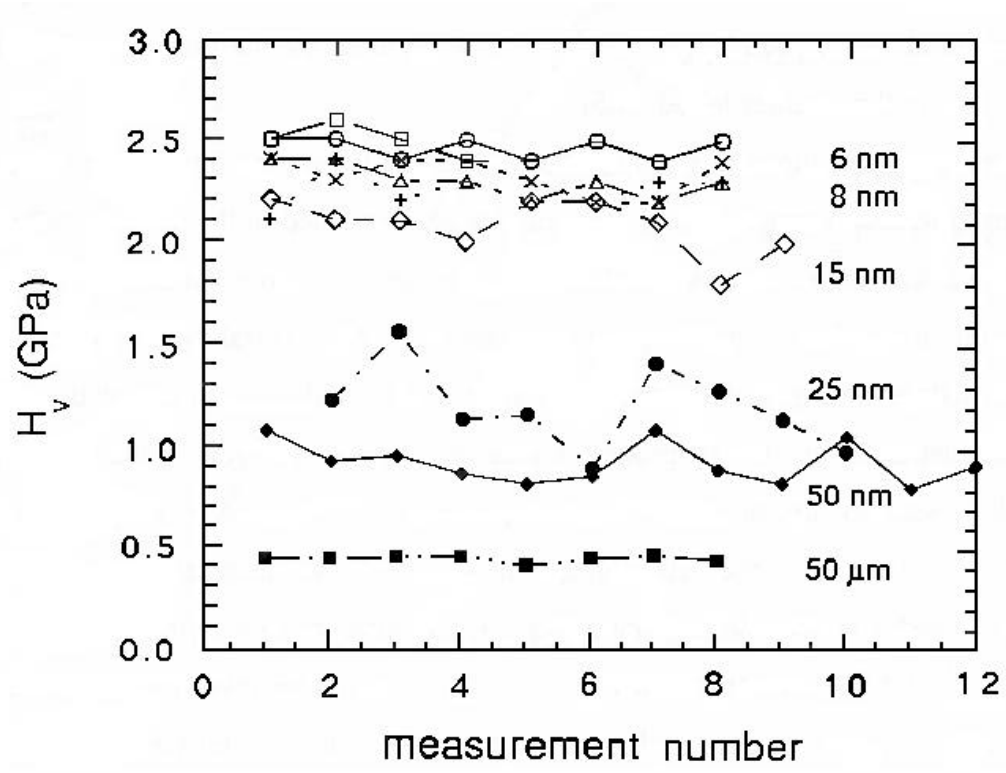


Fig. 7. Microhardness (Vickers) Measurements across nanophase Cu samples ranging in grain size from 6 to 50 nm and compared with conventional 50 µm grain size Cu. [1]

### 2.4.2 Tensile Strength and Fracture

Face-centered cubic metals tested in tension have exhibited similar improvements in strength as those seen in their hardness behavior, but they have shown limited ductility. The limited levels of ductility exhibited by nanophase metals may arise because of difficulties in creating, multiplying, and moving dislocations, but may as well relate to the presence of significant flaw populations in these materials. The results to date on the fracture properties of nanophase materials have been limited in scope and hindered by the presence of porosity or interfacial phases in the samples tested. [55] Conventionally brittle ceramics have been observed to become ductile, permitting large plastic deformations at low temperature if the ceramics are generated in the nanocrystalline form. Doping of nanocrystalline ceramics has been demonstrated to reduce grain growth dramatically. Grain boundary sliding, grain rotation and grain shape accommodation by diffusional processes seem to play a crucial role in the deformation of nanocrystalline ceramics, i.e. processes that are typical for superplasticity. [56]

It appears that the increasing hardness and strength in nanophase metals with decreasing grain size is simply a result of diminishing dislocation activity and increasing grain boundary density. Fig. 8 shows how the frequency of dislocation activity decreases and that of the grain boundary sliding increases. [1]

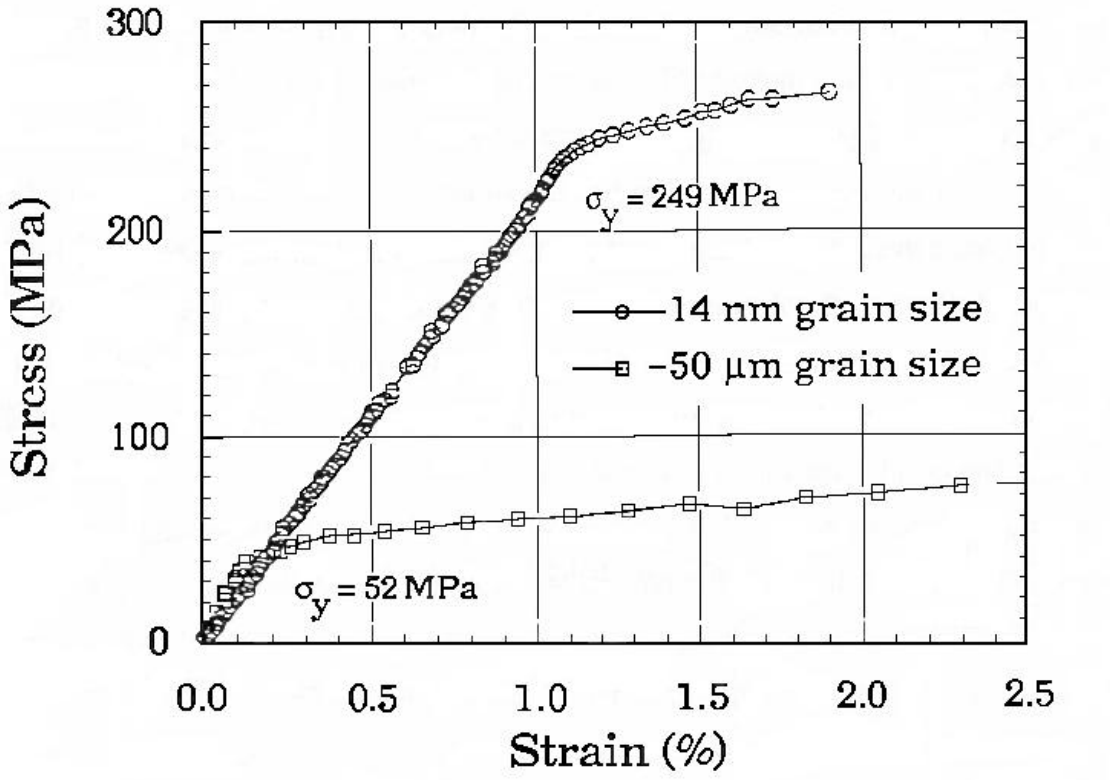


Fig. 8. A stress-strain curve for nanophase Pd compared with that for a coarse-grained Pd sample. [1]

Cemented carbides, (a hard material used for making tools), combine the hardness of tungsten carbide and fracture toughness of cobalt. In order to optimize the compressive strength of the material the amount of cobalt has to be adjusted so that both hardness and fracture toughness meet the requirements of the application. The effect of particle size on the material is related to the carbide phase that becomes harder with decreasing particle size [57]. A uniform phase dispersion is crucial in the materials in order to maintain the advanced characteristics.

## 2.5 TRANSPORT PROPERTIES

The solid oxide fuel cell is a candidate for efficient electric power generation systems. Solid electrolytes used in such cells have been under increased investigation for many years due to their suitability as ionically conductive materials at high temperatures, such as solid oxide fuel cells and oxygen sensors. A considerable amount of research is being carried out in order to develop materials suitable for applications in the medium temperature range. [58]

These solid electrolytes have mostly fluorite structure. Open structure is required for the material to have high ionic conductivity. The IVB group oxides $ThO_2$, $CeO_2$, $PrO_2$, $UO_2$ and $PuO_2$ have the fluorite structure and by doping it is possible to stabilize this structure for $ZrO_2$ and $HfO_2$. The addition of dopants gives rise to the creation of oxygen vacancies responsible for the ionic conductivity in these oxides. [59]

### 2.5.1 Ionic and Electronic Conductivity

There are two important ways in which materials can conduct electrical current. Both electrons and ions can carry electric charge. For metals, the electronic conductivity dominates while for many ceramic oxides ionic conductivity is the major contributor that may exceed electronic conductivity by several orders of magnitude. In metals the non-localized electrons carry the charge. The ionic conductivity is associated with ion motion. Lattice defects are of great importance for ionic conductivity [60]. Diffusion and ionic conductivity are related through the Nerst-Einstein equation.

By doping cerium oxide, it becomes an anionic conductor at high oxygen pressures. Lower valent cations in the lattice make the formation of anion vacancies energetically more favorable than the formation of electron holes. At intermediate oxygen pressures n-type conductivity interferes [59].

### 2.5.2 Effects of Particle Size and Doping on Electrical Conductivity of Ceria

Transport properties of ceramics, in semi- and ionic conductors, are often limited by grain boundaries. The defect and transport properties of nanocrystalline oxides are unique in two principal aspects. Grain boundary impedance is greatly reduced which is attributed to size-dependent impurity segregation [61]. In varistors for example this gives rise to useful electrical barriers. Defect thermodynamics dominated by interfaces are obtained in a bulk material when particle size is in the nanometer regime. The unusual defect thermodynamics of the nanocrystals are attributed to interfacial reduction [62]. The heat of reduction of nanophase ceria is lowered by more than 2.4 eV per oxygen vacancy compared to coarse particles. This reduction occurs at suitably low-energy to dominate the nonstoichiometry and electrical conductivity of the material as whole.

Diffusion usually takes place by the movement of ions to neighboring vacancies. Oxygen atoms are located in the oxygen interstitials on non-fluorite sites. For stoichiometric compounds, the vacancy concentration and ionic conductivity are very small, but suitable doping may increase both. Also, smaller particle size increases the non-stoichiometry of a material. The oxygen ion conductivity of doped cerium oxide with a constant doping level has been found to be dependent on the lattice constant of the compound. Low levels of doping changes the conductivity of ceria from an ionic to an electronic conductor. [63]

# 3. MATERIALS INVESTIGATED AND SYNTHESIS METHODOLOGY

## 3.1 Materials Investigated

This thesis covers studies on several different properties of nanophase materials including; oxides and carbon/carbide materials. The structure-property relationships were studied for three metal oxide materials. In addition, during the laser ablation of molybdenum in hydrocarbon atmosphere the formation of carbide clusters as well as the formation of fullerenes or organic polymers was noted depending on the hydrocarbon used in the ambient gas.

### 3.1.1 Oxide Materials

#### 3.1.1.1 Silicon Oxide

Silicon oxide, silica, is one of the most intensively studied materials due to its wide application in the semiconductor industry. α-quartz is thermodynamically the most stable form of silica at room temperature. The structure is built from helical chains of linked tetrahedras. Amorphous silica is obtained by slowly cooling molten silica, and shows no long-range order but a disordered array of chains, sheets and three-dimensional units. Fumed silica is a very fine white smoke of amorphous silica. It has very low bulk densities and high surface areas. [74]

Most modern technology is based on silicon semiconductors. Suitable band gaps are achieved by doping silicon with group V elements, such as As and Sb, or with group III elements, e.g. Al or Ga, in order to obtain n- and p-type semiconductors, respectively. One field where silicon is not used is on luminescent displays and diodes. Nanophase silicon materials may make this application possible.

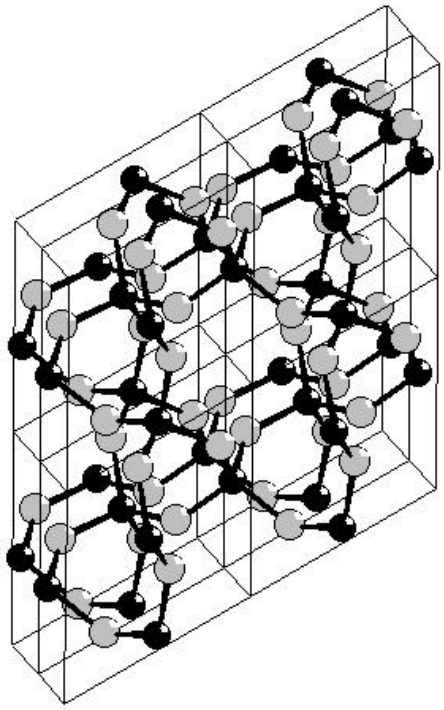

Fig. 9. Crystal structure of $SiO_2$.

Quantum size effects and chemical nonstoichiometry cause silicon and silica, to emit photoluminescence. By tuning the size and composition, new kind of diodes can be developed, as the use of one excitation wavelength can give rise to different colors.

### 3.1.1.2 Iron Oxides

Iron forms several oxides, with oxidation state II (FeO) and with oxidation state III ($Fe_2O_3$), or a mixture of both ($Fe_3O_4$). FeO has a cubic rock salt structure. The black powder is metastable disproportionating at temperatures below 575°C but can be obtained under rapid cooling. $Fe_2O_3$ is reddish-brown and has two modifications, namely α and γ. The α-form has a hexagonal close packed structure of oxygen ions and metal ions in the octahedral sites. γ-$Fe_2O_3$ has a cubic close packed structure of oxygen ions and the metal ions occupy sites that give trigonal inverse spinel structure (spinel structure is shown in Fig. 4). [74]

γ- $Fe_2O_3$ is extensively used in magnetic recording tape and disc manufacturing. [75] It is used as such or mixed with other metals e.g. cobalt. γ- $Fe_2O_3$ is a permanent magnet material, and is stable at ambient temperature. The demand of increasing recording density has created materials science research in order to decrease the domain size, but keep it stable towards thermal fluctuations. The lower limit for magnetic domains is about 30 nm. Oxidation of iron causes enormous economical losses. The rusting of iron causes corrosion and billions of dollars are spent yearly to replace damaged iron. This poor stability is the reason why iron metal is not so widely used in magnetic recording.

### 3.1.1.3 Cerium Oxide

Cerium oxide has a relatively high free energy of formation. Cerium dioxide, or ceria, is the most stable form of cerium oxides. Trivalent $Ce_2O_3$ is not stable in air or water. $CeO_2$ has a face centered cubic (fcc) crystal structure.

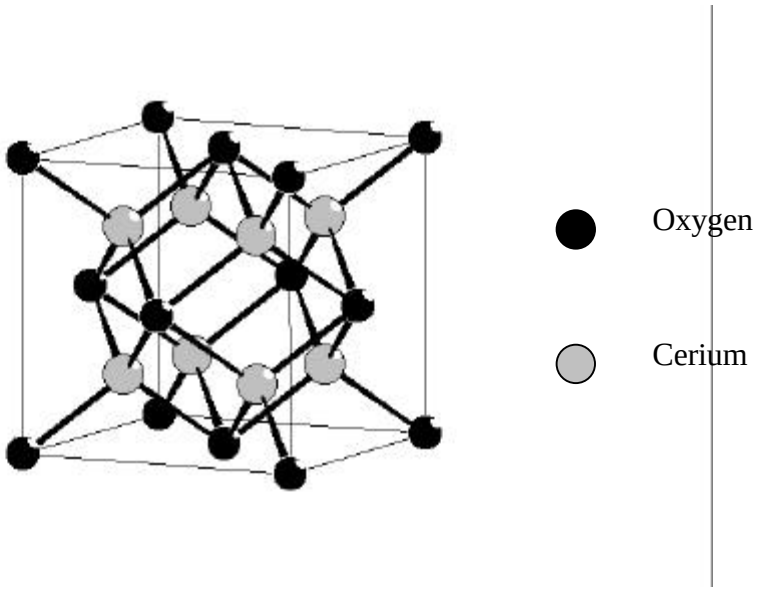


Fig. 10. Crystal structure of $CeO_2$.

Ceria is used in car exhaust catalysts as an oxygen storage buffer. Due to the ease of change of oxidation state ($Ce^{3+}/Ce^{4+}$) it can store and release oxygen under different operation conditions. Ceria can improve the function of the catalysts through transport of oxygen into the oxide structure and back to the noble metal due to enhanced ionic conductivity properties of ceria through oxygen vacancies.

In this thesis, materials where some of the cerium atoms (5-80 atom-%) in $CeO_2$ structure were replaced by atoms with lower (e.g. Ca, Nd and Pb) or equal (Zr) valence state were synthesized in order to create controlled oxygen vacancies. By decreasing the particle size and doping the ceria fluorite structure, higher catalytic activity can be obtained. Studies on improving the oxygen storage capacity and catalytic activity have been performed. Models were applied in order to understand the parameters determining the properties.

### 3.1.1.4 Spinel Structure

Spinels have the general chemical formula $A^{III}{}_2B^{II}O_4$, with a crystal structure of cubic close packed oxygen ions and divalent ions in the tetragonal sites and the trivalent ions in the octahedral sites. They are made up of $AO_4$ and $AB_4O_4$ units. Spinels are commonly used as catalysts for high temperature applications. Spinels may catalyze combustion reactions and are especially effective for the reduction of nitrogen oxides. Analogously to ceria, the creation of a mobile oxygen sub-lattice is of great importance. Good ageing stability is required in order for spinels to function effectively as catalysts.

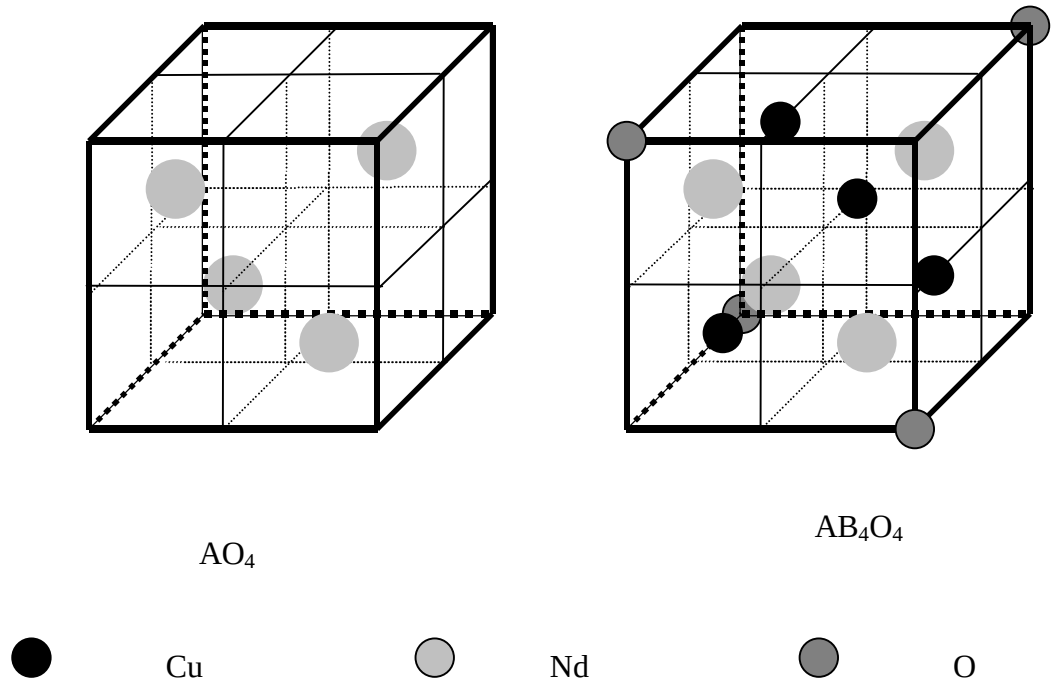


Fig. 11. Crystal structure of $Nd_{1.5}Ca_{0.5}CuO_4$ spinel.

In this thesis, some spinel compositions were synthesized and catalytic activity for conversion of hydrocarbons and CO was studied. Neodymium was chosen as ion A and Cu as ion B. Part of neodymium was substituted with calcium. The cerium doping of the spinel was also studied. However, neodymium doped $CeO_2$ is so stabile that we the doped spinel structure could not be obtained.

### 3.1.2 Carbon Compounds

#### 3.1.2.1 Fullerenes

The third allotropic form of pure carbon, the so-called fullerenes, was discovered in 1985 [76] in experiments where graphite was evaporated in vacuum using the laser ablation technique. Later, other techniques e.g. carbon arc [77] were developed to prepare macroscopic quantities of fullerenes. Fullerenes are a family of carbon clusters of different sizes. They have a hollow carbon cage structure. The most stable cluster is $C_{60}$, but there are others at higher molecular weights. The smallest fullerenes $C_{60}$ and $C_{70}$ have very high molecular symmetries, $I_h$ and $D_{5h}$, respectively. The cages consist of twelve pentagons and a suitable number of hexagons. Energetically the most favorable are the structures where pentagons are separated. In large fullerenes ($n \geq 76$) there is more than one isomer that fulfills this requirement. In general, large fullerenes prefer low-symmetry structures separating the pentagons as far apart as possible [78]. The structures of $C_{60}$ and $C_{70}$ are shown in Fig. 12.

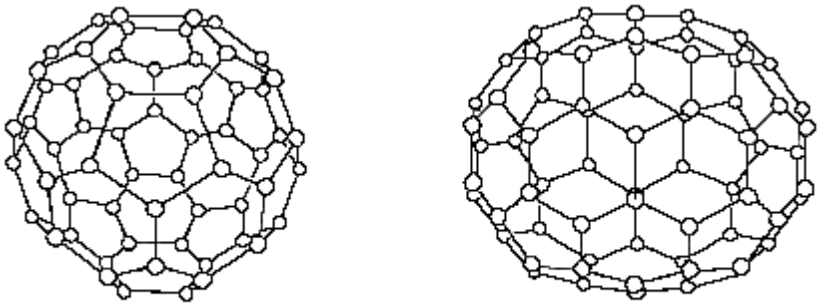

Fig. 12. Perspective views of $C_{60}$ (left) and $C_{70}$ (right).

After being formed in inert atmosphere fullerenes are fairly stable in air. In the gas phase fullerenes do not react with NO, CO, $SO_2$ and $NH_3$ and react only slowly with $H_2$ and $O_2$ [79]. Fullerenes have higher oxidation reactivity than other forms of carbon [80] (diamond, graphite and soot). Unlike these other forms of pure carbon, fullerenes are soluble in nonpolar organic solvents like benzene, and they can be separated using chromatography [81]. A solution of $C_{60}$ is quite reactive.

Because there are no double bonds in pentagonal rings the electron delocalization is poor and gives rise to a high reactivity. $C_{60}$ is more similar to a giant closed-cage alkene than an aromatic molecule. Fullerenes decompose in light via oxidation by oxygen or ozone. Fullerenes are unable to undergo substitution reactions. The chemistry of fullerenes is similar to alkenes [82]. Fullerenes have a cage diameter of ~ 7Å which allows them to capture one [83] or more [84] atoms (usually lanthanoids) into the cage. The notation $M@C_{60}$ is used to specify that the metal atom is inside the fullerene cage. A stable close-shell derivative of $C_{28}$ [85] has been obtained by encapsulating $U^{4+}$ ion inside, $U@C_{28}$.

Fullerenes form interstitial compounds with alkali metals that show superconductivity up to 30 K. $T_c$ is shown to increase with increasing unit cell size (Fig. 13.) [86]. The transition temperatures are lower than those for ceramic high temperature superconductors but are higher than for conventional superconductors. Superconductivity is thought to arise because of the coupling of purely intramolecular $C_{60}$ modes. A decrease in the bandwidth and an increase in the density of states drives the change in $T_c$ as the $C_{60}$ molecules are moved farther apart. The observed isotope effect suggests that pairing mechanisms involving only electronic interactions are unlikely for these materials and phonons are important [87].

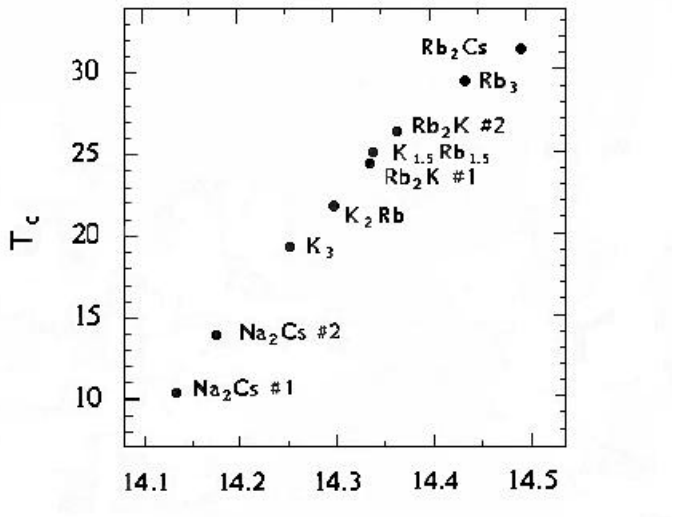


Fig. 13. $T_c$ (K) versus cell size of superconductive $A_3C_{60}$. [86]

### 3.1.2.2 Met-cars and Other Metal Carbides

Met-cars were discovered when the catalytic activity of titanium in olefin polymerization was studied [88]. A $Ti_8C_{12}$ peak at 528 amu was much more intense than any other peak. Met-cars have been found to form in reactions of titanium with several different hydrocarbons. The met-car structure (Fig. 10) was determined with $^{13}C$ substitution when the mass peak shifted up to 12 amu. No hydrogen was found in isotope labeling. Same structure was seen in $V_8C_{12}$, $Zr_8C_{12}$ and $Hf_8C_{12}$ but not for cobalt and tantalum [89].

Cluster growth does not lead to the enlargement of the cage size but multicage structures are formed [90]. Double cage $Zr_{13}C_{22}$ and $Zr_{14}C_{21/23}$, a triple cage at $Zr_{18}C_{29}$, and a quadruple cage at $Zr_{22}C_{35}$ have been observed. Test have shown that met-cars are extremely stable with regard to oxygen reactions, but chemical reactions with polar materials added exactly eight polar molecules like ammonia and alcohol to each cluster. To be so reactive, all the metal atoms have to be on the surface of the cluster. It has not been possible to prepare these clusters in macroscopic amounts.

Not all metals form met-car structures, molybdenum for example was found to form a cluster with another structure [91], when molybdenum carbonyl was irradiated with XeCl laser. Molybdenum carbide clusters, $Mo_nC_{4n}^-$ ions are extremely nonreactive with $NH_3$, $H_2O$, and $O_2$. This suggests structures in which the molybdenum atoms are unavailable for coordination to additional ligands. A structure where a planar cluster of two, three, or four

molybdenum atoms is surrounded by, and bonded to, carbon dimers is shown in Fig. 14. Correspondingly, it has not been possible to prepare macroscopic amounts of a cluster based carbide material.

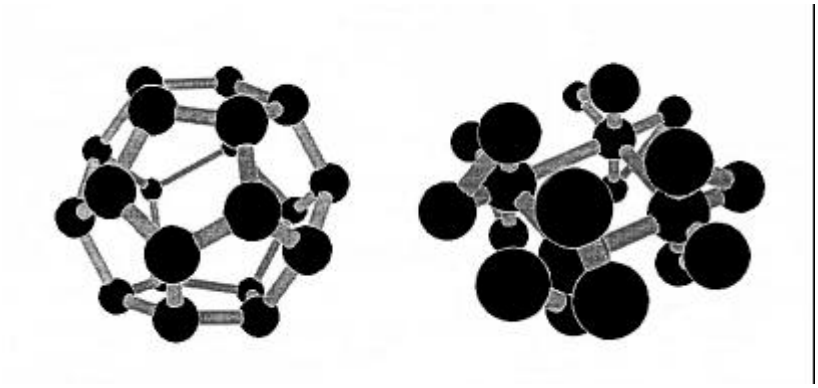

Fig. 14. Structures of met-car and $Mo_4C_{16}$ cluster [91].

## 3.2 Methods of Synthesis

Nanophase materials are highly reactive because of their large surface to volume ratio. However, for developing improved performance of the materials, interesting properties are obtained when combining the size with tailored chemical composition. Nonstoichiometry can be achieved by preparing materials under such conditions that the stoichiometric composition is not formed or by introducing non-isovalent ions into the crystal structure. Nanoparticles are made under conditions were these phases are stable e.g. in vacuum under rapid cooling, or with methods where the growth of particles can be restricted. Techniques for the generation of nanoscale clusters or particles in this thesis represent two different groups: Gas-phase evaporation-condensation and precipitation from solution.

Generally, materials with high purity can be produced by gas phase condensation, although in smaller quantities. Chemical methods, on the other hand, are suitable for producing larger quantities of material. However, contamination of the surface by ions from solution may be a problem. A brief description of these two approaches to produce nanoparticles is presented below.

### 3.2.1 Preparation of Nanoparticles Using Inert Gas Evaporation - Condensation

Gas phase condensation methods include evaporation of elemental materials using ovens [4, 64] and laser beams [65-67] and thermal decomposition of metals from their precursors by pyrolysis. Nanoparticles grow from supersaturated vapors. In order to obtain the required properties, a desired particle size and narrow size distribution are needed, which requires a good understanding of factors determining the particle growth.

Instead of conventional heating, [4, 64] evaporation is achieved by a laser pulse ($CO_2$, Nd: YAG or Excimer laser) that ablates metallic [65,66], and oxide [67] targets. Within a very short time scale, the surface of the target is locally heated to extremely high temperatures. Therefore, this technique enables endothermic reactions to take place. Pulsed lasers are preferred because continuous lasers heat up the target too much and may melt it. The resulting plume contains mostly neutral atoms, which are cooled by collisions with the carrier

gas. This results in supersaturation and cluster growth. Metal densities are usually low enough, so that the growth is dominated by successive monomer additions. Cluster size distributions are characteristically broad as a result of changes in vapor pressure [68]. Rapid particle growth is observed if the amount of vapor is increasing. Big particles are also obtained since coagulation of particles is enhanced while coalescence is retarded further away from evaporation point.

In principle, this method is capable of preparing nanoparticles of any material using one or several targets. By this approach, it is possible to mix metals that do not normally form alloys. Gas phase reactants can also be used in laser synthesis of nanoparticles [69-71]. Volatile compounds like organometallic, metal carbonyls or metal hydrides are decomposed using continuous lasers to prepare metal particles. Ethylene and ammonia have been added to prepare metal carbides and nitrides, respectively. If the reactants do not absorb enough laser radiation inert sensitizer, like $SF_6$, can be added. The method is continuous and controllable with laser power and reactant flow rate. Heating and cooling rates are controllable as well as the maximum temperature of the plume and can be tuned to tailor the properties of the particles.

#### 3.2.1.1 Principles of Cluster Growth in Gas Phase

The critical step in the particle formation process, is the formation of a stable nucleus since atoms on the surface are not as stable as those in the interior of the particle. The conventional nucleation theory for homogeneous nucleation is used to explain particle formation from gas phase through two phase transitions to solid phase. The free energy per atom is given by

$$F_n / n = (m_p - m_n) + a * \sqrt[3]{n} . \qquad (1)$$

where $\mu_p$ and $\mu_v$ are the atomic free energies in the bulk and in the vapor, respectively, The second term represents the surface free energy per atom in a particle of size n where n is the number of atoms in the particle and $\alpha$ is a constant [72]. In order to form stable particles, the vapor must be supersaturated, i.e. $\mu_v > \mu_p$ and n must be large enough so that the magnitude of the first term in Eq. (1) is larger than the second term. It follows that, a critical diameter, D* must be achieved before a particle becomes stable. The critical diameter is given by

$$D^* = 4x \frac{1}{rRT \ln(p_v / p_0)} \qquad (2)$$

$\xi$ is the surface energy
$p_v$ is the partial pressure of the vapor
$p_o$ is the equilibrium pressure of the atoms at the temperature T
$p_v/p_o$ is the supersaturation ratio
Typical values for the critical diameter of nuclei predicted by equation (2) are rather small, 1nm or less, as a result of the rapid cooling of the vapor.

Once stable particles are formed, supersaturation rapidly decreases quenching further nucleation. At low supersaturation, particles grow bigger since the number of nuclei is lower and the additional material is deposited on the fewer particles present. Particle growth changes its character quickly from initial monomer addition to Brownian coagulation. At first, where the temperature is high enough to allow the agglomerated particles to coalesce keeping the particle spherical. As the temperature decreases it leads to the formation of agglomerates. Agglomeration leads to a log normal distribution as presented by Granqvist [64]. If the density of particles is relatively low and the time before the particles are collected

is relatively short then the particle agglomerates are small. Methods are usually developed so that hard necking between particles is avoided.

### 3.2.2 Preparation of Nanoparticles Using Chemical Methods

Chemical methods are widely used for synthesis of multi component metal oxides. The most important solution chemistry methods to prepare nanoparticles are co-precipitation and sol-gel techniques. This thesis deals with coprecipitation method, where metal ions are precipitated as organometallic compounds. Thermal treatment can also be seen as chemical grinding because during decomposition, the evolved gases also break the particles decreasing their size. The coprecipitation method is relatively easy to scale up. The main advantage of precipitation, in comparison to solid state reaction methods is that it rejects most of the impurities to the solution during the formation of solid product. Particle formation in solution chemistry follows the same fundamentals as in the gas phase synthesis. A short description of particle growth is given below. A more detailed description of the process can be found in reference [73].

#### 3.2.2.1 Nucleation

The precipitation involves nucleation, where the driving force is the change in chemical potential between standing and equilibrium states. The most common method to generate supersaturation is by reactive precipitation, when a chemical reaction produces insoluble species. The supersaturation in precipitation is often very high, giving high nucleation rates.

Nucleation is the least understood process in precipitation. Unlike in laser vaporization where homogeneous nucleation dominates, three main types of nucleation occur in chemical precipitation: Primary homogeneous or heterogeneous or secondary. Homogeneous nucleation occurs in the absence of solid interface while heterogeneous nucleation occurs in the presence of foreign seed surfaces and secondary nucleation in the presence of a solute particle interface. The dominance of each type of nucleation varies with the precipitation conditions.

In homogeneous nucleation of small clusters a large fraction of atoms is present at the surface of the particles thus having higher potential energy than in the interior of the particles due to fewer and weaker bonds. The free energy of these small aggregates is the result of free energy due to the new surface and the formation of new solid.

Most nucleation in precipitation methods is in practice likely to be heterogeneous since contact with vessel, stirrer etc is difficult to avoid. Nucleation on a foreign surface has a lower surface energy leading to a lower critical supersaturation. Secondary nucleation results from the presence of crystals in solution and can be divided into three classes: apparent, true and contact. Apparent refers to small fragments washed from the surface of seeds. True secondary nucleation occurs due to the presence of particles in solution. Contact secondary nucleation occurs when a growing particle contacts walls, stirrer, etc. producing new particles. Contact nucleation is often the most important nucleation mechanism and depends on rotation speed, particle mass density and saturation ratio.

### 3.2.2.2 Particle Growth

After a particle is nucleated, it can grow by several different mechanisms. The kinetics of the growth mechanisms determine the structure and particle size distribution. On a macroscopic level, mass transport usually limits the particle growth while heat transfer is so fast that it controls the growth only at a very high heat of crystallization. Diffusion controlled growth is described by diffusion of solvated ions to the surface and diffusion of solvent and other coordination ions away from the surface.

The supersaturation driving force can be written as S-S(r*) if the particles are small. If S-S(r*) is positive a particle will precipitate from solution and when S-S(r*) is negative particles smaller than size r will dissolve and particles larger than r* will grow. This dissolution of fine particles and re-precipitation of larger particles is called Ostwald ripening. Ripening occurs in batch reactors because the supersaturation ratio, S, decreases with time. At high supersaturation nucleation produces large numbers of fine particles.

Impurities can change the crystal habit drastically, especially ionic surfactants which by adsorbing on the surface of a crystal can change the kinetics. Impurities can reduce the supply of material to the surface, reduce the specific surface energy or block surface sites. Ionic surfactants adsorb on the surfaces with opposite charge and can limit the growth of particles in some directions.

### 3.2.2.3 Agglomeration

In chemical methods, the agglomeration time is long compared to the confined growth zone in vaporization methods. Normally crystals do not occur as single discrete units but they form bigger clusters. There are two main classes of agglomeration; primary agglomeration results from the faulty growth of crystals and secondary growth is due to crystal-crystal interactions. There are two cases of secondary aggregation. Particles can aggregate by Brownian motion or shear induced aggregation. In the first case, the diffusion of particles by Brownian motion causes collisions and in the latter case fluid movement causes particle collisions.

### 3.2.2.4 Drying

The precipitation methods involve separation of solid phase from the liquid reaction media. Drying requires simultaneous heat and mass transfer. These processes are dependent on the temperature and partial pressure of the solvent in the atmosphere. Depending on the kinetics of the drying of the boundary layer surrounding the green body and the pores different stresses are induced in the material. The wet green body has a compressive capillary force, which holds it together. During drying, this capillary induced tension is present if flows keep the surface wet. This flow arises from the rearrangement of particles in the green body. This capillary force disappears as the liquid is evaporated. During drying the green body is susceptible to non-uniform stresses due to the pressure gradient of the flow of liquid during shrinkage and the escaping gases or the differential thermal expansion of the ceramic due to temperature gradients in the green body.

# 4. EXPERIMENTAL METHODS

## 4.1 Preparation Methods

### 4.1.1 Experimental Set-up for Laser Vaporization

A schematic diagram of the modified diffusion cloud chamber used in this study is shown in Fig. 15. This equipment is a modification of the upward thermal diffusion cloud chamber [92].

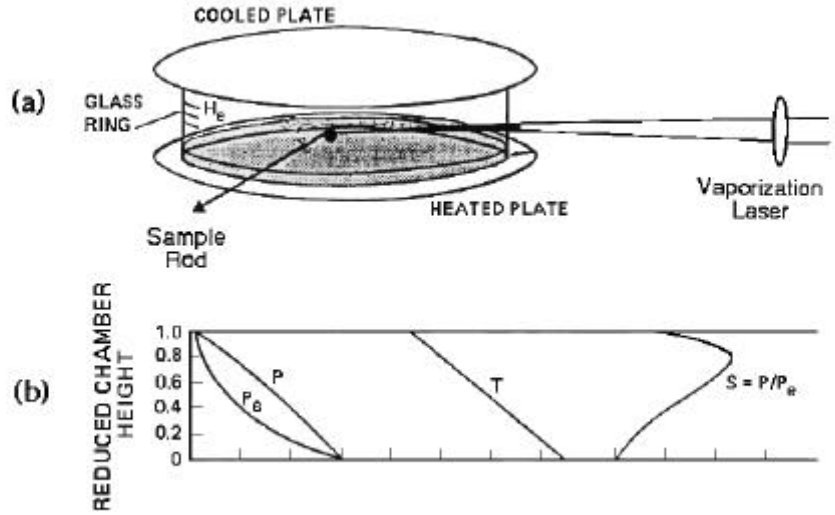


Fig. 15. (a) A diagram of the diffusion cloud chamber, (b) temperature and pressure profiles in the chamber.

The chamber consists of two horizontal circular stainless steel plates, separated by a circular glass ring. Nichrome heater wires are wrapped around the glass ring and provide sufficient heat to prevent condensation on the ring and to maintain a constant temperature gradient between the plates. A metal target is placed on the bottom plate and the temperature of the target and the plate are maintained at a temperature higher than that of the upper plate. The top plate can be cooled to less than -100$^{o}$C by circulating liquid nitrogen. The bottom plate can be heated up to +100$^{o}$C by circulating boiling water. Usually the chamber is filled with a carrier gas such as He or Ar and with some reactant gas (e.g. $O_2$ for oxides and isobutylene or ethylene for carbides) so that the total pressure is 800 Torr. A rotary pump is used to evacuate the chamber. The large temperature gradient between the plates results in a steady convection current which can be enhanced by using a heavier carrier gas such as Ar or Kr under high pressure conditions (1-1000 Torr).

A Nd: YAG laser (Quantel) was used to vaporize the metal of interest. The second harmonic wavelength (532 nm) was pulsed at 20 Hz and had an energy of 20 mJ per pulse. The beam was directed to the target using three prisms. In the preparation of mixed oxides, the beam was split into two using a semitransparent beam splitter. A quartz lens with a focal length of 50 cm focused the laser beam. With the help of an adjustable lens the laser beam could be moved to a fresh surface during a run. An atomic metal vapor was created containing a

fraction of ionized metal atoms. Due to the low yield of the synthesis (about 1%) experiments were typically run for two hours. A few milligrams of oxide or carbide were generally obtained.

This technique was mainly used to prepare metal compounds rather than pure metals e.g. oxides and carbides. The hot metal atoms react with $O_2$ (in oxides syntheses) to form vapor-phase metal oxide molecules that undergo several collisions with the carrier gas, thus resulting in efficient cooling via collisional energy loss. From the total pressure employed in the experiments, it is expected that the metal atoms and the oxide molecules approach the thermal energy of the ambient gas within several hundred microns from the vaporization target. The unreacted metal atoms and the less volatile metal oxide molecules are carried by convection to the nucleation zone. The temperature profile is expected to be a linear function of elevation in the chamber. Since the equilibrium vapor pressure ($P_e$) is approximately an exponential function of temperature, the metal oxide vapor can easily be supersaturated (supersaturation $S = P/P_e$, where P is the actual partial pressure of the metal oxide in the chamber) in the nucleation zone near the top plate (figure 15).

Supersaturation can be controlled by increasing the temperature gradient between the plates. The higher the supersaturation, the smaller the size of the nucleus required for condensation. Therefore, by controlling the temperature gradient, the total pressure and the laser power (which determines the number density of the metal atoms released in the vapor phase), it is possible to control the size of the condensing particles. The particles formed in the nucleation zone are condensed on the top plate during the run. The chamber was allowed to warm up to room temperature, and the particles were collected under atmospheric conditions.

### 4.1.2 Preparation of Nanoparticles Using the Coprecipitation Method

True coprecipitation of mixed metal precursor crystal involves the precipitation of metals as salts with a specific stoichiometric ratio of the metals. Another possibility for precipitation of multi component systems is simultaneous precipitation and coaggregation. In this case mixing is not on the atomic level. The scale of mixing depends on the relative rates of nucleation, growth and aggregation in precipitation. In our case the precipitation occured through simultaneous precipitation.

In the coprecipitation method, metals were precipitated as oxalate compounds, which were thermally decomposed to oxides. The interfacial tension of the solid, which depends on pH and ionic strength of the precipitation medium control the growth of particle size. [16] The higher the pH and ionic strength, the smaller the resulting particle size.
Computer modeling (using CEC and Hydro programs) was used to optimize precipitation conditions for the doped cerium oxide synthesis. Sufficient thermodynamic equilibrium data was available for all the metals studied except zirconium. For zirconium an experimental study was made and an approximate solubility constant for zirconium oxalate was determined. Fig. 16 shows an example of equilibrium calculations for zirconium precipitation as oxalate as a function of pH.

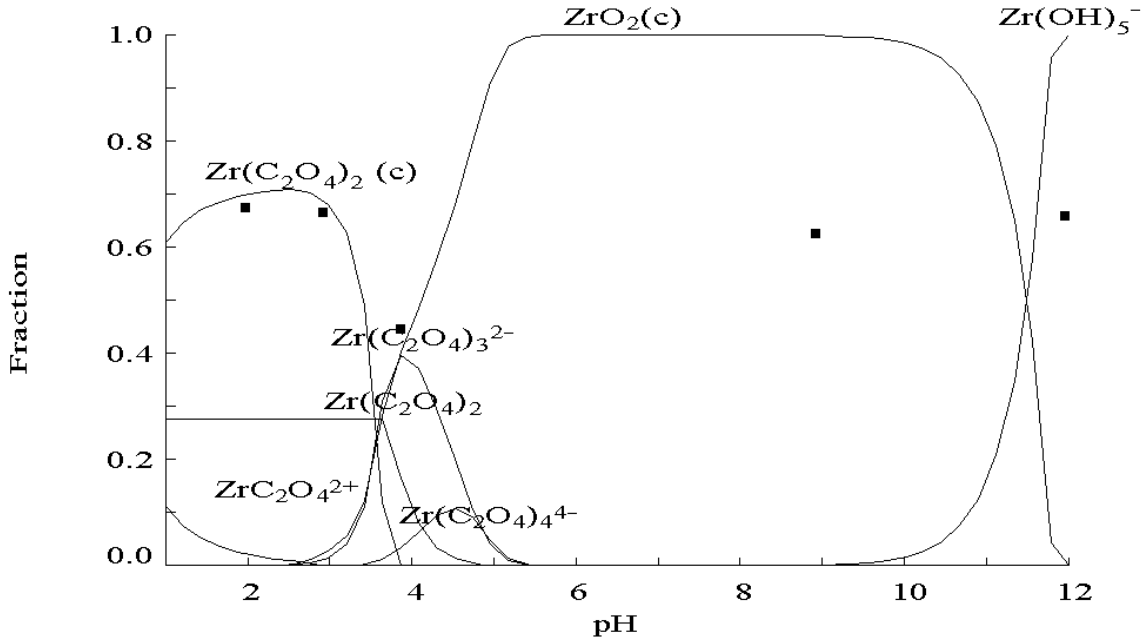


Fig. 16. Precipitation of zirconium as oxalate as a function of pH plotted as fraction of oxalate ion. Experimental results for zirconium precipitation are represented by the black squares.

## 4.2 Characterization Methods

### 4.2.1 Transmission Electron Microscopy

Transmission electron microscopy (TEM) is a good tool to study the particle size, morphology and crystal structure. Samples do not need to be conductive unlike in SEM and STM. TEM gives a good resolution down to a nanometer scale. In TEM there is the possibility of obtaining electron diffraction patterns to identify the crystal structure as well as to use EDX to study the local chemical composition of the samples. In this work, a JEOL 2000 EX instrument was used combined with LZ-5 EDSX detector.

### 4.2.2 Raman / Infrared Spectroscopy

In nanosize powders the surface species absorption can compete with the absorption of the bulk species. Therefore, the characterization of these powders cannot be complete without the identification of the surface chemical species. FTIR can be utilized to analyze the surface contamination. Typically there will be contamination from atmospheric $CO_2$, water and hydrocarbons. Especially oxide surfaces that are always more or less hydrolyzed can easily adsorb water molecules and $CO_2$ to form carbonate species.

Infrared spectra were recorded using Nicolet 750 Magna Fourier transform spectrophotometer. The sample chamber was purged with dry air for about ten minutes before scanning. The energy range for measurements was 400-4000 $cm^{-1}$ and the resolution 4 $cm^{-1}$. Samples were mixed with potassium bromide and then ground and pressed to pellets.

### 4.2.3 SQUID Magnetometer and AC- susceptometer

The superconducting quantum interference device (SQUID) was used for magnetic characterization of nanoparticles at DC fields. The Quantum Design $MPMS_2$ instrument with a superconducting magnet can be operated using fields up to 9000 G and measurements can be performed at temperatures 1.7 - 350 K. The system makes use of a second order derivative coil configuration to eliminate the effect of stray fields. The sample chamber is at a low pressure of helium gas, which provides thermal contact with a flow of gas outside the sample chamber pipe that is used to change and stabilize the temperature. Over 4.5 K flow impedance and a gas heater take care of the temperature control.

The temperature is homogenized around the sample space by copper wires. Two kinds of measurements were performed. In zero-field cooled operation mode, the sample was cooled to 5 or 10 K at zero field and 20 Gauss field was applied and the temperature dependence of magnetization was recorded. This measurement was followed by a field-cooled scan when the sample was cooled down at 20 G field. The blocking temperature ($T_b$) of the nanoparticles was determined from the zero field-cooled measurements as a temperature for the onset of the superparamagnetic state to be at the temperature of maximum magnetization. In field-cooled measurements the blocked, constant magnetization starts to decrease.

Hysteresis loops were measured at the desired temperatures starting from zero Gauss up to 9000 G down to -9000 G and back to 9000 G. Between all the loops the sample was heated to 300 K and the remanence field was minimized using an oscillating magnetic field. A scan length of 4 cm was used in all measurements.

AC magnetic measurements were performed using a home-built AC-susceptometer with a three-coil mutual-inductance-bridge. The sensitivity of the instrument was approximately $10^{-7}$ emu. Measurements can be performed over a wide temperature range from 4 to 350 K. Fields up to 1000 Oe can be applied at low temperatures and up to 200 Oe at room temperature. Background correction is done by regularly removing the sample from the secondary coil and measuring the signal without a sample. The driving field was 3 Oe for all measurements and the frequency was varied from 4 Hz to 4 kHz.

### 4.2.4. X-Ray Diffraction

X-ray diffraction analysis was used to study the crystallinity of powder samples. This method can be used for phase identification, grain and unit cell size determination. Several Guiner cameras and diffractometers were utilized in these studies but in all cases Cu $\alpha 1$ radiation with wavelength 1.5405 Å was used. For the Guiner films, a scanner system was used to read the films and process the data.

For grain size determinations Scherrer's equation (3) was used. Samples calcined at 800 °C were used as a standard with no line broadening. For each sample, all lines were used and the average of the particle size was taken.

$$d = \frac{K \cdot l}{b \cdot \cos q} \qquad (3)$$

### 4.2.5 X-ray Photoelectron Spectroscopy

The surface chemistry study of the nanophase oxides and reaction mechanism for cobalt reduction on tungsten carbide surface in polyol process was performed using the XPS technique. The surface composition and contamination were studied at room temperature. Reduction and oxidation studies were also made at elevated temperatures.

The data was acquired using a PHI-5500 ESCA system from Perkin-Elmer using 300 W Al Kα monochromatic radiation. The oxidation and reduction experiments below 550 °C were performed in an ultrahigh vacuum reaction chamber connected directly to the XPS chamber. The oxidation of the samples was carried out in a 1% $CO_2$/He atmosphere of 1.3 kPa, while the reduction experiments were executed under an 8% $H_2$/Ar atmosphere of 1.3kPa. Oxidation at 550 °C and 600 °C was performed outside the XPS reaction chamber. The spectra were curve-fitted using a software package developed by Perkin-Elmer. Mixed Gaussian-Lorenzian functions were used to approximate the peak shapes. In the tungsten carbide – cobalt interface study additional spectra were collected using synchrotron radiation at 157 eV with very short free mean path in the solid, resulting in extreme surface sensitivity.

### 4.2.6 Catalytic Testing of Powder Samples

An apparatus was constructed to study the catalytic activity of ceramic powder samples and this is shown in Fig. 17. Gas flow was adjusted to 25000 $h^{-1}$ using Bronkhorst digital mass flow regulators. The flow consisted of oxygen and a CO/propene mixture in stoichiometric ratio and using helium as the carrier gas. A packed-bed quartz micro-reactor was used and it was mounted in a vertical furnace (Eurotherm 94D). The reactor was heated to 600°C at a rate of 5°/min. Analysis of the out-going gases was performed using a Spectra Minilab analytical 300D masspectrometer. Typically 50 milligrams of sample was used for measurement. Firstly helium gas was purged for two hours in order to determine the lower base line with no reactants in the flow. Each sample was measured three times in order to get reliable results and the average of the 50% conversion was taken.

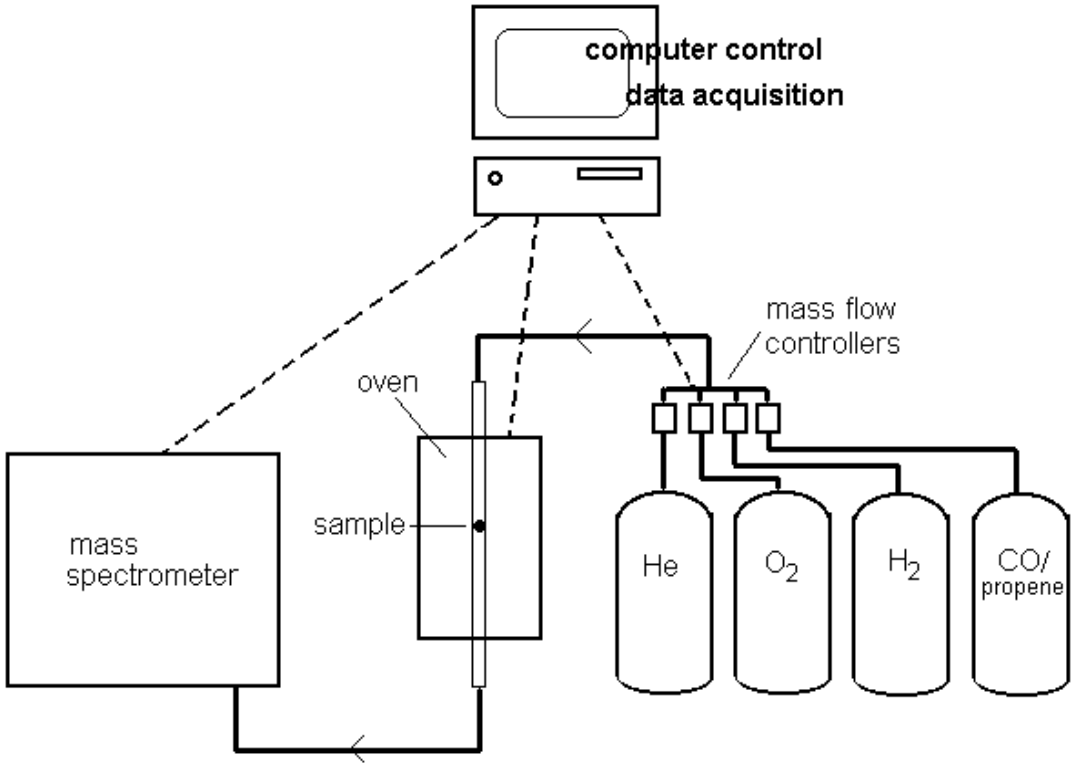


Fig. 17. A schematic drawing of catalytic reactor set-up.

### 4.2.7 Temperature Programmed Reduction

TPR measurements were performed using a Micromeritics TPD/TPR 2900 analyzer with a thermal conductivity detector. 10 % $H_2$ in argon was used to reduce the samples.

### 4.2.8 $CO/O_2$-pulse Experiment

The oxygen storage characteristics and catalytic activities of the materials during dynamic redox conditions, similar to those in a car engine, were studied. The catalyst inlet temperature was set at 500 °C. Pulses of oxygen alternated with intervals of 2, 5, 10 and 40 seconds with pulses of carbon monoxide were injected through the heated model catalyst. Two lambda sensors (Bosch, 0 258 104 001, type LSM 11), were used to measure the oxygen concentration. The concentrations of outgoing CO and $CO_2$ were measured by CO/ $CO_2$ NDIR analyzers. $N_2$ was used as carrier gas at 1000 Nl/h. The space velocity was 25 000 $h^{-1}$.

### 4.2.9 Oxygen Chemisorption Experiment

The oxygen storage capacity of the samples during static redox conditions was studied using oxygen chemisorption. The drill cores of the catalysts were heated to 400 °C and reduced with hydrogen gas (4 vol-%, 6 l/h), then purged by $N_2$ gas for 15 minutes. At the same

temperature, oxygen pulses of 60 s (2 vol%, 1 l/h) were then introduced at five minute intervals, until no more oxygen was chemisorbed. Nitrogen was used as a carrier gas at 15 l/h during both reduction and oxidation. The outgoing oxygen concentration was analyzed using a paramagnetic analyzer, Oxynos 100.

### 4.2.10 Model Catalyst Tests

Model gas test equipment was used to evaluate the catalytic performance of cerium oxide samples deposited on monoliths under conditions close to the real operation. The hydrocarbons were detected with a Flame Ionization Detector RS 55. The $NO/NO_x$-analyzer came from Beckman Industrial, Model 951 A. IR UV/VIS Binos Gas analyzers were used to determine the concentration of $CO/CO_2$ and $SO_2/NH_3$, for oxygen determination an Oxymat paramagnetic analyzer from SIEMENS was used. Hydrogen concentration was measured with a Leybold Hydros 1 TCD.

The light-off temperature for CO, NO and hydrocarbons, during rich and lean fuel conditions, was investigated. The temperature of the catalyst was increased to 500 °C at a rate of 20 °C/min. The space velocity of the inlet gases was 100 000 $h^{-1}$. The inlet gas composition for rich and lean conditions is shown below. $N_2$ was used to balance the gas mixture. The air-to fuel ratio was changed from between 0.9800 to 1.0200.

*Table 2. Gas composition used in model gas tests.*

| Component | **Rich (vol-%)** | **Lean (vol-%)** |
|---|---|---|
| **CO** | 1.40 | 1.40 |
| **$H_2$** | 0.47 | 0.47 |
| **$O_2$** | 0.928 | 1.771 |
| **$C_3H_6/C_3H_8$ 2:1** | 0.10 | 0.09 |
| **NO** | 0.10 | 0.10 |
| **$CO_2$** | 14.0 | 14.0 |
| **$H_2O$** | 10 | 10 |
| **$SO_2$** | 20 ppm | 20 ppm |

Two lambda-sweep tests, one static and one dynamic, were made to determine the conversion ratios and the lambda windows of the catalysts. The gas composition used was the lean mixture and the tests were performed at 400°C. The oxygen concentration was changed linearly from 0.928 to 1.771 vol% and back. During the dynamic sweep tests, additional $O_2$-pulses with a frequency of 0.5 Hz were introduced for a ± 0.87 A/F perturbation. The space velocity was 100 000 $h^{-1}$.

# 5. RESULTS

## 5.1 New Structures and Materials

In the laser vaporization synthesis some interesting agglomeration morphologies were observed. The prepared materials often had nonstoichiometric structures giving rise to new materials properties. Some cluster carbides were prepared for the first time in macroscopic amounts. The formation of larger fullerene structures was enhanced in preparation of fullerenes using molybdenum as a catalyst. All these results will be described in this chapter.

### 5.1.1 Web Morphology and Nonstoichiometry of Oxides

Using laser evaporation in the upward thermal diffusion cloud chamber at high pressures of reactive and carrier gases, different oxides, carbides and to some extent nitrides, as well as pure metals were prepared. Metal atoms reacted readily with other molecules present in the gas phase during the nucleation and cooling processes forming the required compounds directly thus no post treatment, e.g. carburization or oxidation, was needed. The particles formed were mostly very small, typically below 10 nm, as seen in TEM micrographs in papers I-III, and V. Some larger particles were also formed probably due to the pressure shock waves in the laser preparation which makes particles grow much larger. The number of these particles was low. Nanoparticles agglomerated and formed favorable web-like structures as seen in the SEM micrograph in paper I. A possible growth mechanism of these self-arranged web structures could arise from a nucleation mechanism of the nanoparticles from the vapor phase on the cold substrate surface. Structural defects at the interfaces of the nanoparticles could promote the nucleation of the observed agglomeration pattern. At lower temperatures, it is possible that the nanoparticles can identify these surface defects and thus self-arrange themselves into the observed morphology. At higher temperatures, the surface defects can be completely annealed and no such structures form. These two things; small particle size and the web-like structures give very high surface areas, for example $SiO_2$ had a surface area as high as 460 $m^2/g$.

The photoluminescence emission for the silica structure was observed and the spectrum contained two broad peaks at 467 nm (2.64 eV) and 422 nm (2.94 eV) and the origin of the peaks can be related to the defects in the $SiO_2$ structure (Fig. 18. and Paper I). It is proposed that this $SiO_2$ center is present in significant amounts in oxygen-deficient silica. This conclusion was also supported by the data obtained with time-resolved photoluminescence in amorphous silicon dioxide. We have to assume that the laser ablation of x-Si in oxygen as described here resulted in a silica nanostructure with a large concentration of defect $SiO_2$, especially at its surfaces, which in turn gave rise to the observed bright photoluminescence. The removal of oxygen from $SiO_2$ results in Si-Si bonding across the resulting oxygen vacancy, but on further reduction these vacancies organize into extended shear defects. Indeed, the Raman spectrum of the $SiO_2$ particles (Fig. 19) showed a strong and sharp band at 519 $cm^{-1}$, which indicates the existence of Si-Si bonds. The $SiO_2$ defect model was also compatible with the unusually large surface area determined for these silica nanoparticles.

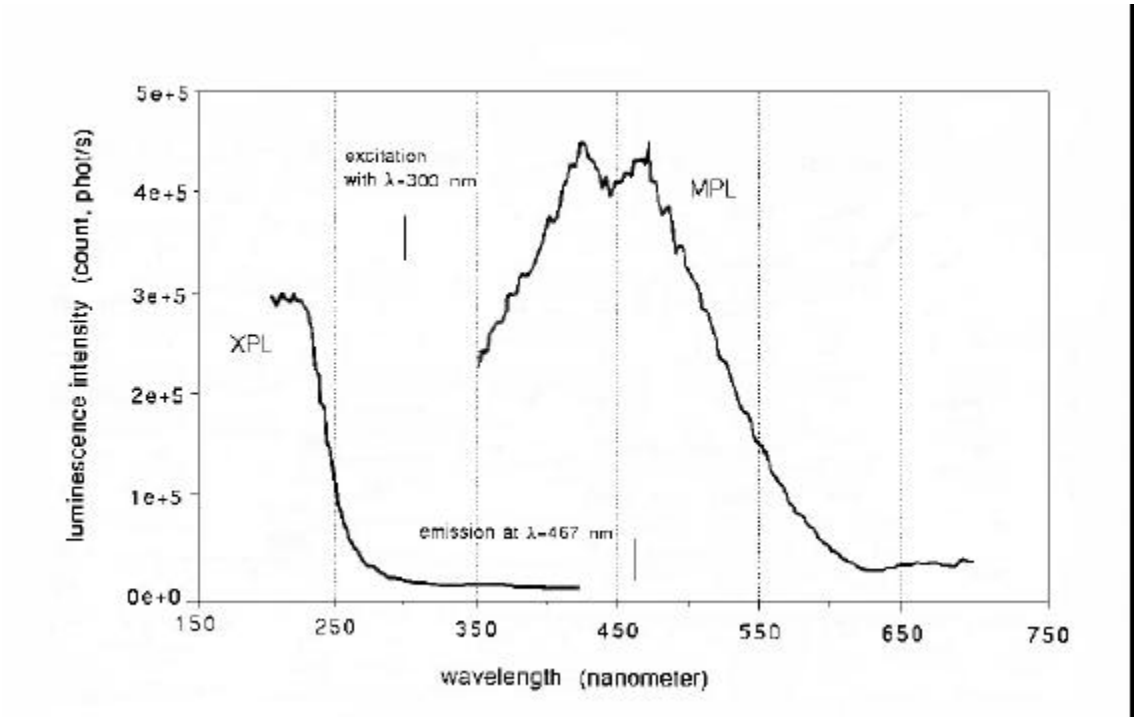


Fig. 18. Photoluminescence spectra of web-like silica nanoparticles at 77 K in emission and excitation modes.

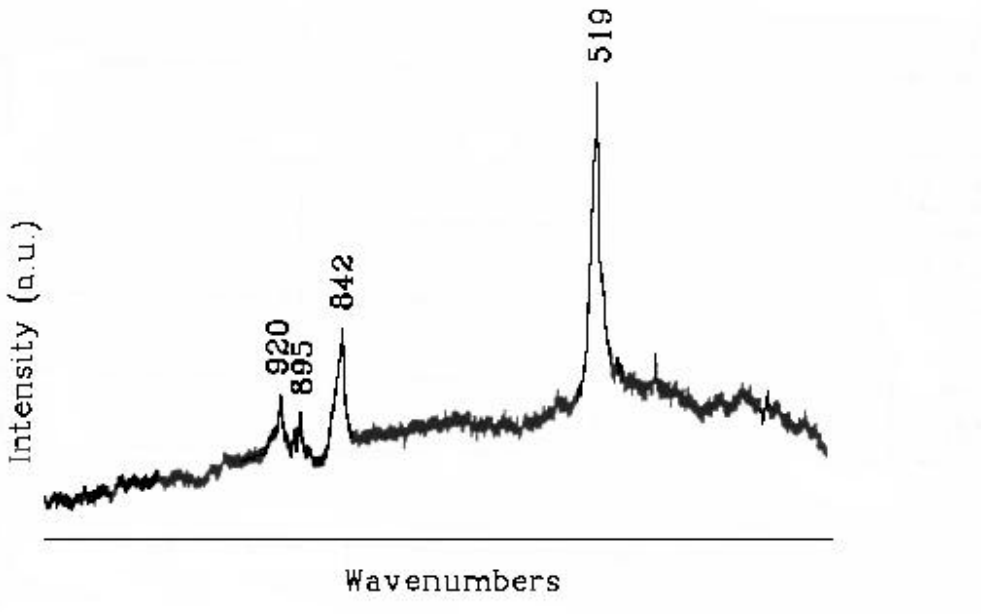


Fig. 19. Raman spectrum of silica nanoparticles.

An alternative explanation for strong photoluminescence in nanoparticle systems is quantum confinement in Si particles. Substantial energy shifts sufficient for emission at 2.7 eV require a particle size below ≈ 4 nm, which is smaller than that observed in the TEM images. However, quantum crystallites could be covered with an amorphous surface layer, making them appear larger in TEM images. This explanation is quite unlikely because luminescence

of quantum size silicon has been reported to be red, not blue as was observed on these samples.

### 5.1.2 Molybdenum Carbide Materials

Molybdenum was vaporized using the diffusion cloud chamber in isobutylene atmosphere in order to prepare molybdenum carbide. The metal rich carbides MoC and $Mo_2C$ are the known forms of molybdenum carbide occurring naturally. $Mo_2C$ has not been found in the samples prepared using this method as shown in the mass spectrum (Fig. 20). We can identify the mass peaks of $MoC_n$ series where n goes from 1 to 4 and another series $(MoC_4)_n$ where n also goes from 1 to 4. The origin of MoC, $MoC_2$, and $MoC_3$ peaks is unquestionable but the latter series is ambiguous since $MoO_3$ and $MoC_4$ have the same molecular weight. Most likely this sample was a mixture of molybdenum oxides and carbides because other carbide and oxide species, where the peaks do not overlap, could be seen. Jin et al. [91] have discovered $Mo_4C_{16}$ molybdenum carbide clusters and they have showed the lack of reactivity of $Mo_4C_{16}^-$. The $(MoC_4)_n^-$ ion did not react with $O_2$, $CO_2$, $H_2O$ or $NH_3$. This is not consistent with the hollow-cage met-car structure which adsorbs eight molecules per cage. The lack of reactivity suggests a structure in which molybdenum atoms in carbide are not available for coordination to other ligands. In this experiment it is expected that $Mo_4C_{16}$ clusters were formed in macroscopic amounts.

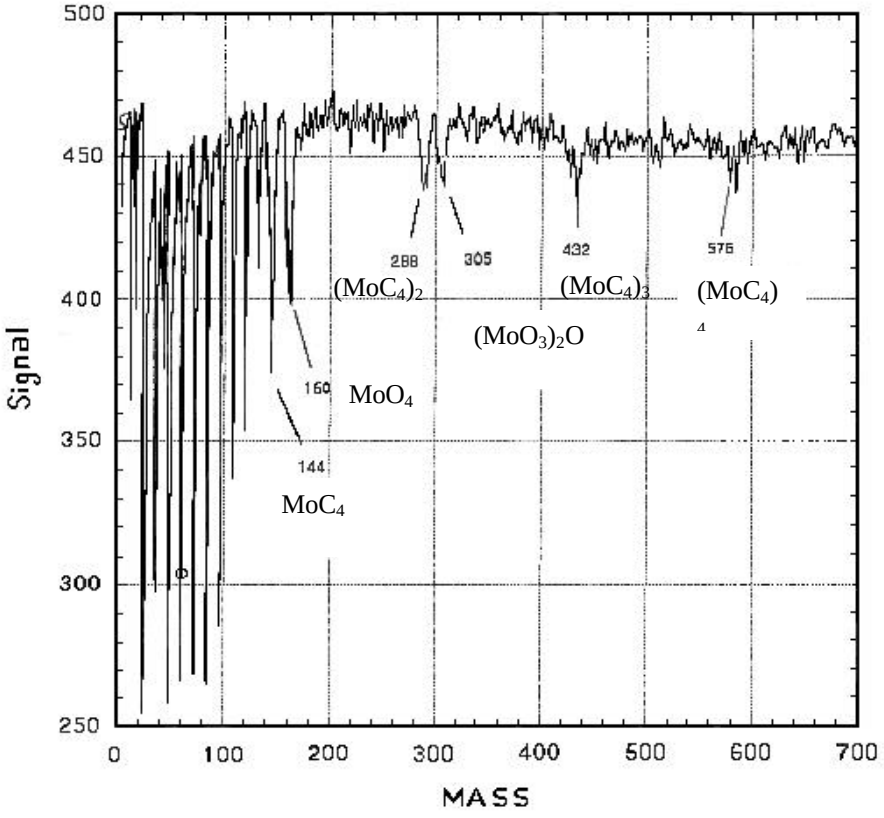


Fig. 20. Mass spectrum of sample prepared by laser evaporation of Mo in isobutylene atmosphere. The presence of $MoC_n$ as well as molybdenum oxides can be seen.

### 5.1.3 Formation of Fullerenes

During the synthesis of molybdenum carbides using the laser vaporization method fullerenes were found to be formed, as seen in the mass spectrum at higher molecular weights (Fig. 21). Unlike other methods of preparation this one seemed to favor the formation of higher fullerenes. In the mass spectrum the presence of $C_{60}$ or $C_{70}$ was not detected but fullerenes of mass number corresponding to $C_{84}$ and up to $C_{150}$ and higher were found. Usually the two smallest fullerene molecules are the most stable ones and dominate the mass spectrum. This indicates that molybdenum had some catalytic effect in the formation of higher molecular weight fullerenes. The evaporation of other metals like silicon did not result in the formation of fullerenes. The organic compound present in the ambient gas also had an important effect on the formation of the resulting product. When ethylene was used as the carbon source in the reaction, the UV-visible spectrum of the soluble product was totally dominated by the polyethylene spectrum and no indication of the presence of fullerenes could be found.

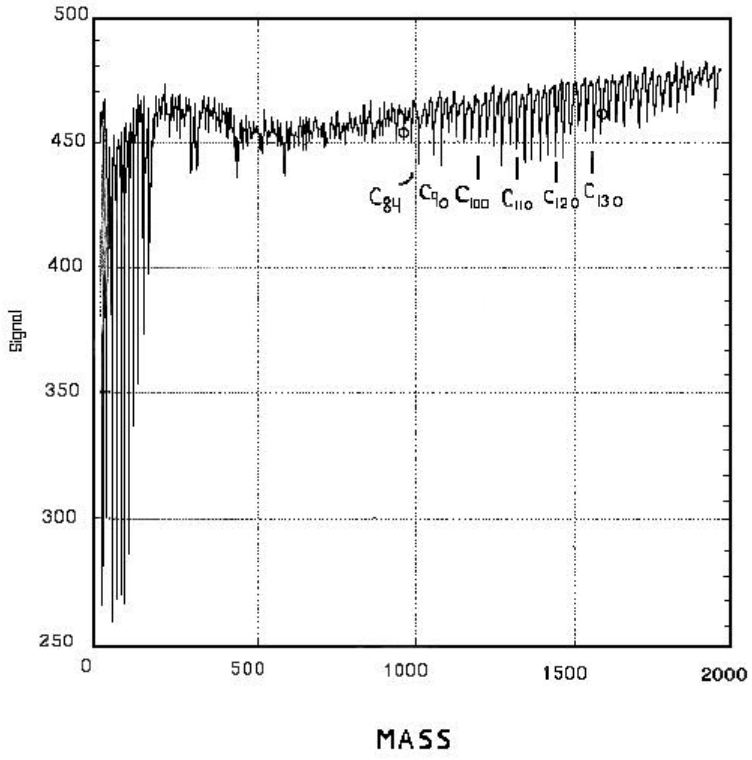


Fig. 21. Mass spectrum of a sample prepared by laser evaporation of Mo in isobutylene atmosphere. The presence of fullerenes at mass unit above 1000 can be observed.

Fullerenes were separated from each other using high performance liquid chromatography. The experimental set-up consisted of; a silica column (24 cm long, diameter 0.5 cm), eluant n-hexane (flow rate 1 ml/min) and UV detection at 260 or 340 nm. Samples were dissolved either in pure hexane or in a mixture of chloroform and hexane (1:1). In the chromatographic analysis the presence of low molecular weight fullerenes was noted but no large ones. This could be result of the low solubility of the higher fullerenes and they were more soluble in chloroform- hexane mixture than in pure hexane.

In order to understand the reactions in the cloud chamber that result in the formation of polyethylene and fullerenes at least two factors have to be studied; the role of the metal and the hydrocarbon. A review about thermal decomposition of hydrocarbons on noble metal surfaces is presented below. It is interesting that the bigger fullerenes were formed since graphite is the most stable form of carbon allotropes and of the fullerenes $C_{60}$ is the most stable one.

Weisshaar [93] has studied reactions of small hydrocarbons with gas phase transition metals. The reactions of gas phase $M^+$ and $M^{2+}$ are unusual. The monopositive cations are highly reactive often dehydrogenating or demethanating linear alkanes in exothermic reactions at room temperatures. The dipositive cations abstract electrons or hydride anions from alkanes from long range or at close range $H_2$ and $CH_4$ elimination reactions can occur just like for monopositive ions. The neutral atoms are inert to alkanes but Sc, Ti, V, Ni, Zr, and Mo react with alkenes. 4d and 5d metal atoms and ions seem to be more reactive with hydrocarbons than the 3d metals. In all cases, the complicated energetics of low-lying metal states of different electron and spin configuration; the size of valence d and s orbitals; and the character of long-range forces determine chemical reactivity.

Spin is gradually degraded as the quantum number gets smaller when moving from 3d to 4d and 5d series. Both the sizes of the atomic orbitals and their energies influence the strength of metal-ligand chemical bonding. The effective nuclear charge felt by the electron increases from left to right across a transition series stabilizing the d-orbitals relative to the s orbitals. In the 3d series the 4s orbital is much larger than 3d while in the 4d series the differences in size is much smaller and the orbital energies are similar. This enhances the ability of 4d to participate in chemical bonding. The neutral 4d series atoms are chemically more active than 3d atoms. The rate-limiting step in metal hydrocarbon reactions is the insertion of metal to C-H bonds. The electron spin conservation is very important in this process. The $M^+$ ions often have a suitable ground state or they have low-lying excited states that can conserve the spin. The inert metal cations have these excited states at too high energies >1.3 eV or they are not able to form d-s hybridisation to make σ-bonds.

The d-electrons of molybdenum interact with the double bonds of the organic molecules through back bonding. The molecules are adsorbed on the surface as follows and undergo a series of reactions at different temperatures [6].

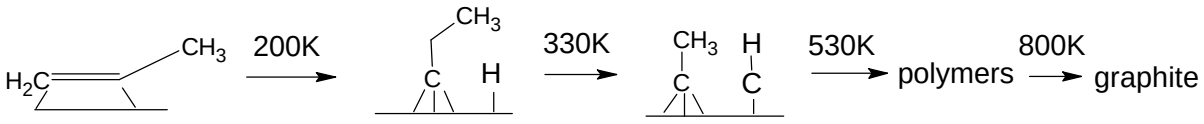


Fig. 22. Thermal decomposition of ethylene and propylene on Rh surface. [6]

The difference in the stability of tertiary and secondary radicals and carbo cations is known, the higher stability of isobutylene radical/cation being explained with steric stability. Also the C-H bond strength is affected the tertiary substitutes having lower bond strength than the lower substitutes. [94]

These three factors could explain, at least partly, why molybdenum catalyzed these reactions and silicon did not as well as the effect of the hydrocarbon used. The formation of higher fullerenes, instead of graphite, could be due to a catalytic effect of molybdenum. The high temperatures of plasma can overcome the high activation energy of formation of these structures.

## 5.2 The Role of Surfaces

In this thesis, two papers were concerned with the surface characterization of nanomaterials. In paper IV the objectives were to study whether the cobalt reduction on a tungsten carbide surface has any catalytic character or not. The emphasis of the ESCA studies in paper VI was to characterize the surface of nanophase oxides regarding the surface contamination related to the different synthesis methods and reduction and oxidation behavior of the samples.

### 5.2.1 Cobalt Reduction on a Tungsten Carbide Surface

The aim of the study of reduction of cobalt on tungsten carbide surfaces was to understand the concept of distribution of cobalt in the carbide matrix and by controlling it achieve homogeneous mixing of the constituent phases. The coating of smaller tungsten carbide particles should be studied in the future since by decreasing the particle size of carbide the hardness can be increased. Homogeneous distribution of Co enables maintenance of the mechanical properties despite the decreased fraction of binder. Since the enhanced reduction rate is based on the change of the nucleation mechanism, instead of catalytic activity of the WC surface, the polyol method can be applied to other systems as well.

Reduction of cobalt using the polyol process was observed to be significantly faster in the presence of a tungsten carbide surface; 5 hours in the presence of WC compared to 24 hours in the absence of carbide (Fig. 23). Reactions involved in the reduction process are complex and not fully understood [95]. The reaction mechanism of the reduction was investigated using surface sensitive X-ray photoelectron spectroscopy.

The measurements were performed in a specially designed ESCA chamber that allows introduction of liquid phase into the chamber and thereby allows studies on solid-liquid interfaces. In the surface studies there was no evidence of the existence of intermediate cobalt complexes on the surface. Therefore it is assumed that Co precipitation in the presence of WC surfaces proceeds through heterogeneous nucleation. $WO_3$ on the surface of tungsten carbide was reduced by hot glycol. It would be of interest to study the effect of particle size of tungsten carbide on the reduction.

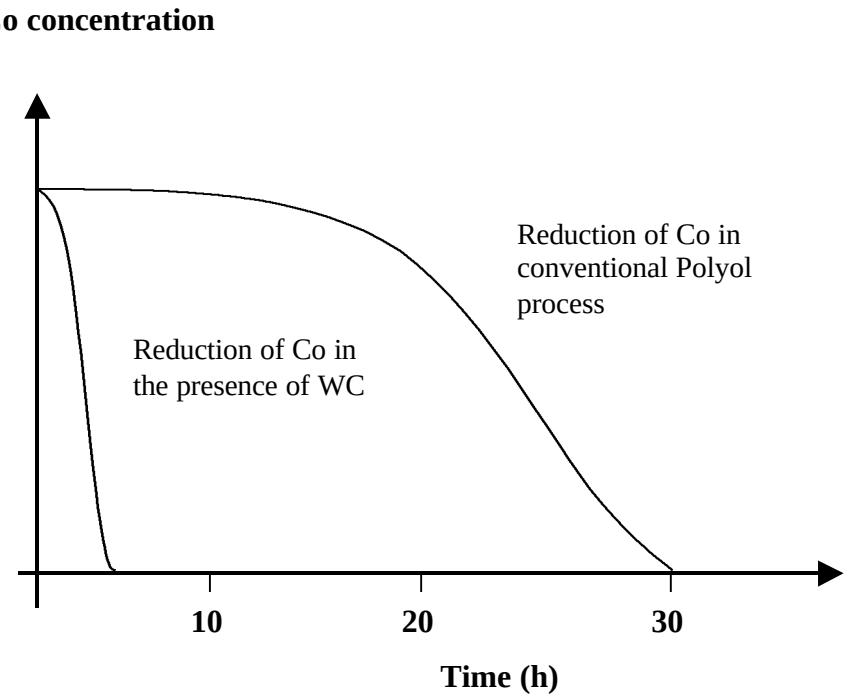


Fig. 23. Reduction of cobalt using polyethylene glycol (polyol process).

### 5.2.2 Surface Study of Zirconium Doped Ceria

The oxygen storage capacity of the zirconium-cerium oxide system has been studied as a function of the composition and the preparation method (paper V). Cerium oxide as mentioned before works as an oxygen buffer in three way catalysts. Zirconium doping gives improved oxygen storage properties and the sensitivity of this property to preparation technique was to be explored. However the fabrication of single phase solid solutions using the selected chemical and physical methods was not quite so straightforward. Higher zirconium content significantly improves the reduction. Maximum reduction capacity was obtained at 20 mol-% zirconium level but at 80% zirconium content even more of the cerium was reduced and the total amount of cerium was decreased. The reduction is shifted to higher temperatures, as zirconium content is increased.

The effect of preparation technique could be compared using the pure cerium oxide samples since the mixed oxides had very different chemical compositions and many inhomogenities. Pure cerium oxide prepared using chemical methods and ball milling showed very similar behavior but laser vaporized $CeO_2$ could be reduced to a much higher extent and at much lower temperatures. From the surface chemical analysis it was concluded that the enhancement originates from surface hydroxylic groups that are present to a higher extent in the laser-vaporized samples.

In the comparison of the different preparation methods for the preparation of cerium-zirconium oxide samples the surface chemistry was studied using XPS technique. The surface contamination was found to be slightly different depending on the preparation method. Samples were observed to have carbon contamination on the surface while no other impurities were observed. In general the carbon concentration was higher for the co-precipitated samples. This could be due to the presence of undecomposed carbonate phase or

could originate from surface charge that enhances the adsorption of carbon dioxide on the oxide surface. The carbon content was not related to the surface area of the samples since laser vaporized samples with the highest surface areas had the lowest carbon contents. Most of the samples had their major carbon peak corresponding to adsorbed C-C or C-H species. Moreover, the samples have another peak that could be related to either carbonate species or O-C-O groups. There were, however, two samples ($Ce_{0.2}Zr_{0.8}O_2$ and the $ZrO_2$ (prepared at pH = 3)), that did not show this emission peak. The higher calcination temperature of the zirconium rich samples could explain the absence of these species either by decomposition of carbonate species or desorption of the O-C-O groups.

a. b.

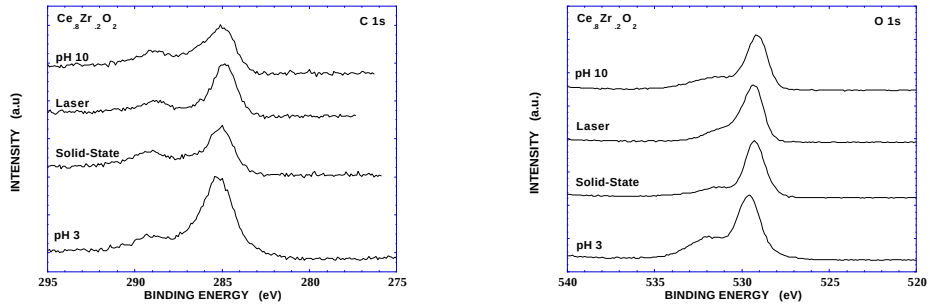


Fig. 24. C1s (a.) and O 1s (b.) emission of $Ce_{0.8}Zr_{0.2}O_2$ prepared by different methods

The O adsorption seems to be related in some way to the presence of Ce as well as to the carbon contamination. The pure cerium oxide samples always had the highest contamination levels. Two oxygen peaks were most profound in the coprecipitated samples (Fig. 24).

a. b.

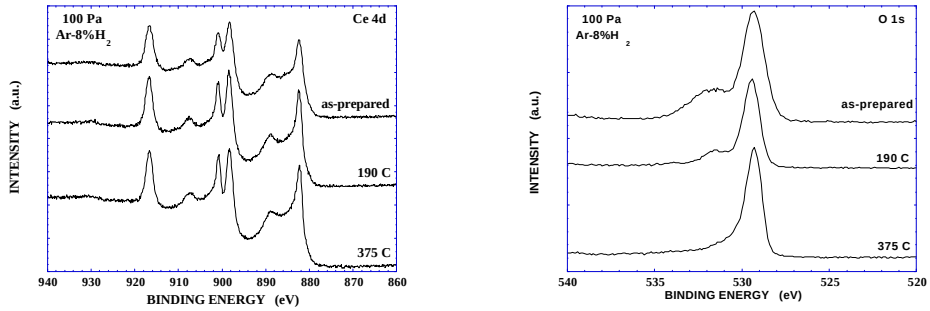


Fig. 25. Ce 4d and O1s emission spectra of coprecipitated $Ce_{0.8}Zr_{0.2}O_2$ as prepared and after reduction at 190 and 375 °C.

The reduction experiments up to 375°C revealed that zirconium stabilizes cerium against reduction since no cerium was reduced at these temperatures contrary to lanthanum doped ceria where reduction was observed already at 200°C [96]. Ce 4d emission was always dominated by $Ce^{4+}$ contribution (Fig. 25a). For the coprecipitated sample some changes in the spectra were observed. The carbon concentration increased whereas the O 1s emission at 531.6 eV was decreased (Fig. 25 b). The reduction process at 375°C was found to be related to the removal of surface hydroxyl groups.

## 5.3 The Catalytic Activity

Doping of nanophase cerium oxide has been shown to affect its catalytic activity. Some dopants can improve the performance while others have a negative effect. The aim of this part of the study was to investigate the effect of the precipitation procedure on the properties of doped cerium oxide. The activity of a model catalyst containing zirconium-calcium doped ceria was investigated and compared to a commercial zirconium doped ceria catalysts. The catalytic activity of different doped ceria samples and a new spinel were studied for car exhaust conversion. Modeling of the catalytic activity as a function of materials properties like heat of formation and acidity was carried out. The results are briefly reviewed below.

### 5.3.1 Effect of Precipitation Procedure on Catalytic Activity of Doped $CeO_2$

The nucleation took place through homogeneous nucleation, since the supersaturation was very high. The agglomerate morphology changed during precipitation. The form of agglomerates changed from spherical clouds to a dense square-like form. From fractal analysis of the agglomerates the agglomeration was shown to proceed through the diffusion limited cluster-cluster agglomeration mechanism.

The effect of the precipitation conditions on properties of oxalates and oxides was studied. Lowering the pH from 3 to 1.5 and change of ammonium ions to protons made the agglomerate size bigger. The addition of anionic surfactant made the agglomerates smaller. The surface area of the dried powder was related to the size of this measured agglomerate size. On the other hand the surface area of the oxides was not directly related to the surface area of the corresponding oxalate. Actually the opposite was true, the lower the surface area of the oxalate the higher the surface area of the oxide.

The particle morphology was affected when precipitation conditions were changed. The synthesis at pH 3 using ammonium oxalate reagent without any other additives produced after a reaction time of one minute a few hundred-nanometer sized amorphous particles without any noticeable micro structure. If reactant solutions were diluted agglomerates with small particles were formed. The addition of a small amount of anionic surfactant had same effect. If more surfactant (2 vol-%) was added needle-like particles became more favorable and at the same time surface area was lost. When ammonium oxalate was changed to oxalic acid particle formation became slower since the kinetics for zirconium precipitation was slowed down remarkably. In this study the collision mechanism was observed in the TEM studies. Collisions of two or three particles were dominant.

The particle growth due to Ostwald ripening affected the particle morphology of the samples in the same way in all the cases. The initial morphology was lost and micrometer size agglomerates were obtained. These agglomerates had thread-like fine structure. The growth rate of the oxalate particles should be related to metal ion concentrations in the mother solution. The remaining cerium ion concentration in the solution was changed from 700 ppm to zero by lowering the pH from 3 to 1.5 or by adding 1 vol-% surfactant. Zirconium concentration was decreased from 300-400 ppm to zero by replacing ammonium ions by protons.

The synthesis of doped ceria was studied and the effect of the precipitation procedure on the ternary oxide was established (Paper VI). The amounts of material synthesized varied from

50 to 100 grams of oxide per batch. The synthesis of zirconium containing powder in large volume caused problems. Single-phase samples were not obtained since cerium and zirconium ions were not homogeneously mixed in the oxalate precursor.

In the study of catalytic activity doped cerium oxide was used as a support and oxygen storage component, noble metals deposited on ceria. Comparison with a standard zirconium doped ceria sample was performed. The addition of calcium into the cerium-zirconium oxide structure improved the oxygen storage capacity of the rhodium catalyst. The lambda window of the ternary oxides (Ce-Zr-Ca) was better than or comparable to the reference sample. Conclusions from the results on oxygen storage capacity and catalytic activity between the different precipitation procedures were difficult to obtain since no correlation between oxygen storage capacity and the observed catalytic activity was observed.

### 5.3.2 Origin of Catalytic Activity of Doped Ceria

Catalytic activity of doped ceria with and without noble metals was studied. Different models were tried in order to establish the relationship between the physical properties of oxide and the catalytic activity (paper VII). Relevant properties related to the activity of catalytic materials include for example acidity and heat of formation of oxide that has been shown to be directly proportional to the heat of adsorption of gas phase components.

Manganese and neodymium-zirconium doping gave the highest activity towards combustion of carbon monoxide and propene in the samples studied. Moreover, neodymium-zirconium doped ceria showed excellent thermal stability up to 1000°C. Undoped ceria in combination with palladium showed high activity. Doping with zirconium or divalent metals did not show any significant improvement of the catalytic performance of ceria.

The light-off temperature, $T_{50}$, defined as temperature at which 50% conversion is obtained, is a measure for the catalytic reactivity of the catalyst. Fig. 26 shows that $T_{50}$ for the carbon monoxide oxidation correlates reasonably well with the surface area of the different sample. For lower particle size the light-off temperature was reduced. The change in the particle size is associated with the selection of dopant since the different samples were prepared in the same way. Surface area was determined by the electronegativity of the dopant. The highest surface area was obtained for samples where the dopant had an electronegativity close to that of cerium.

a.

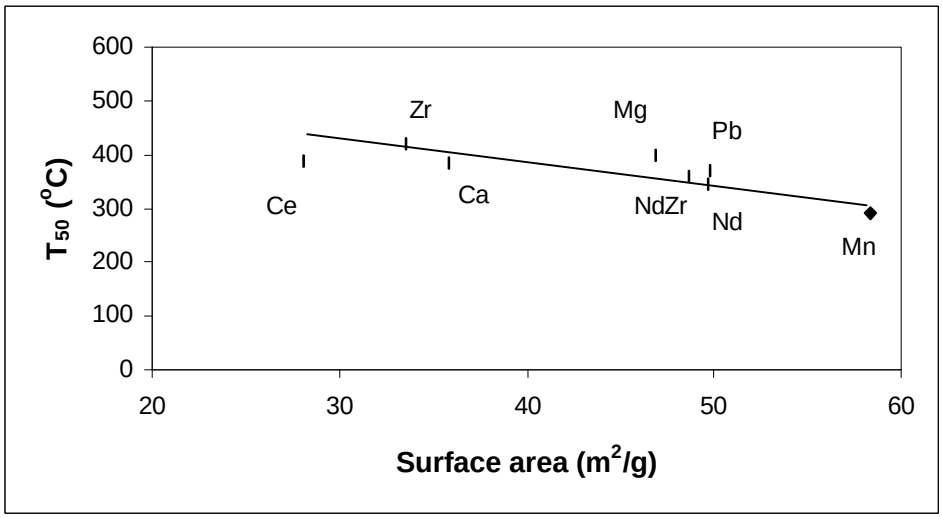


b.

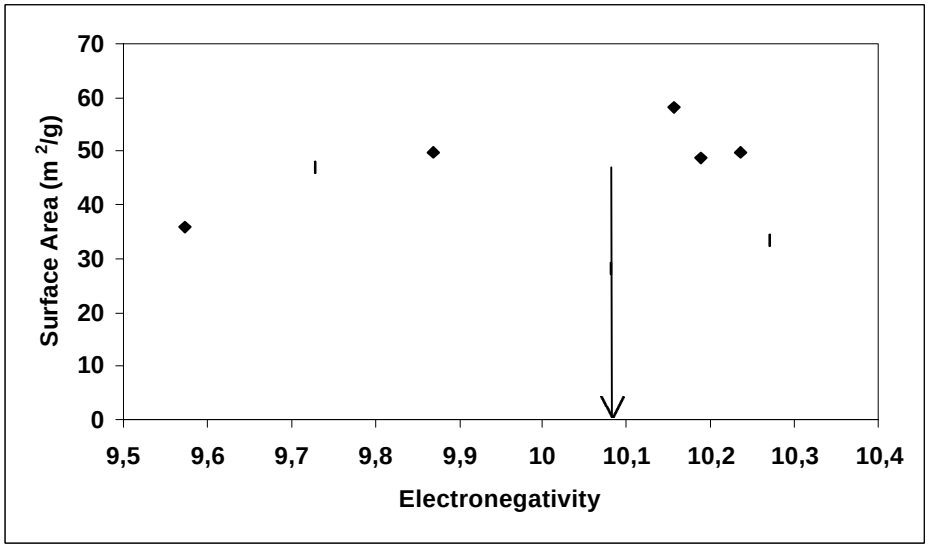


Fig. 26. a. Light-off temperature for carbon monoxide oxidation as a function of surface area, b. Surface area as a function of electronegativity (electronegativity of ceria is marked with an arrow).

The heat of formation of the metal oxide can be used to explain the catalytic activity of doped cerium oxide catalysts (Fig. 27). The heat of adsorption is assumed to be related to the heat of formation of the catalyst oxide. For propene oxidation the lowest light-off temperatures were obtained for samples with highest heat of formation while the opposite was true for oxidation of carbon monoxide. There the lowest ignition temperature was obtained for samples with low heat of formation. These differences could be based on different reaction mechanisms since propene oxidation requires breaking of C-H and C-C bonds while CO is directly ready for oxidation. The Lewis acidity of the support oxide was found to determine the light-off temperature of catalysts containing noble metals both for CO and $C_3H_6$ oxidation (Fig. 28).

The model using the size of the oxygen vacancy can possibly explain the higher ignition temperature for samples containing Ca and Pb that have a vacancy size similar to the size of the oxygen ion with highest bond energies.

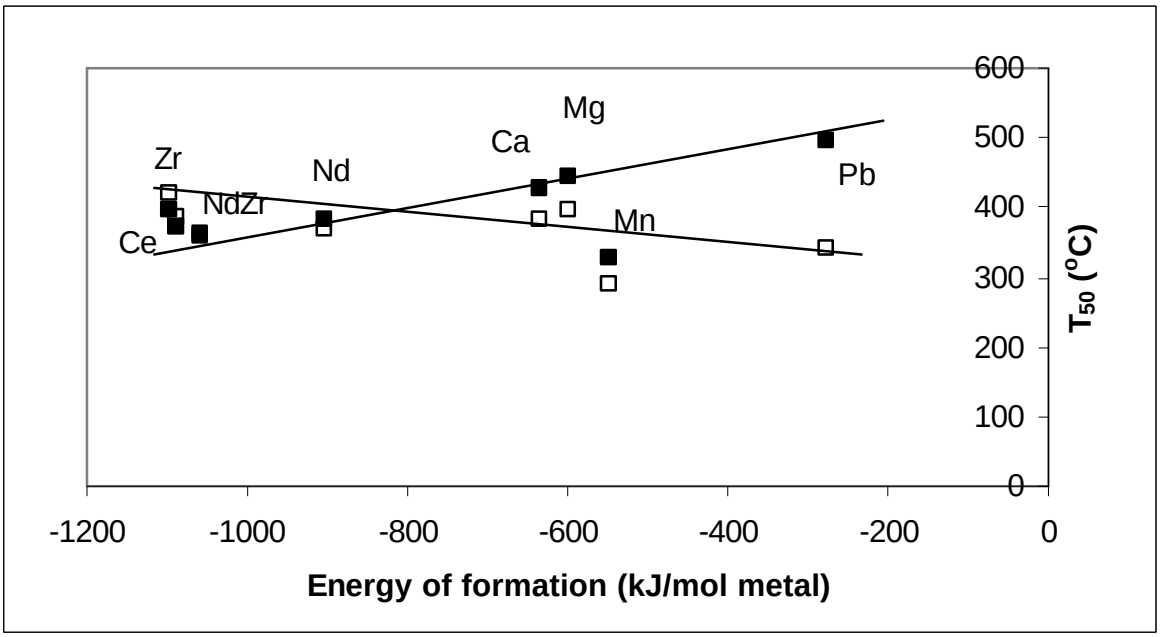


Fig. 27. Ignition temperature for propene (filled squares) and CO (empty squares) combustion on doped ceria catalysts as a function of the heat of formation of the dopant oxide.

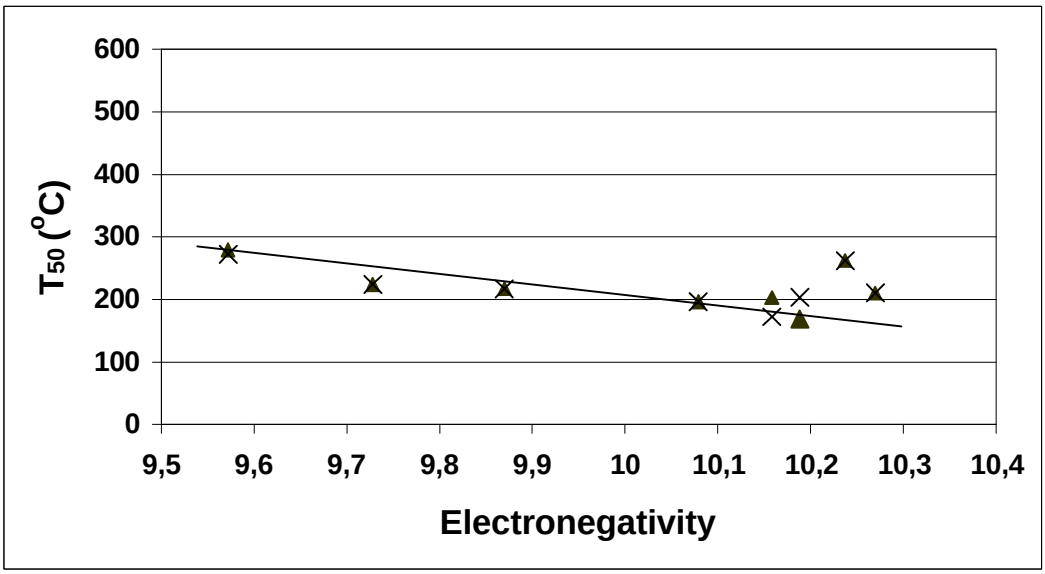


Fig. 28. Ignition temperature for carbon monoxide and propene combustion on palladium loaded doped ceria catalysts as a function of electronegativity.

### 5.3.3 Catalytic Activity of Spinel Samples

The catalytic activity of the spinel structure $Nd_{1.5}Ca_{0.5}CuO_4$ was studied for the oxidation of carbon monoxide and propene under stoichiometric conditions, in the same way as for doped cerium oxide samples. The sample showed good catalytic activity for CO as shown in Fig. 29. However, the use of the sample in subsequent runs showed a significant loss of surface area and the catalytic activity. The particle size for the sample calcined at 800°C was above 500 nm.

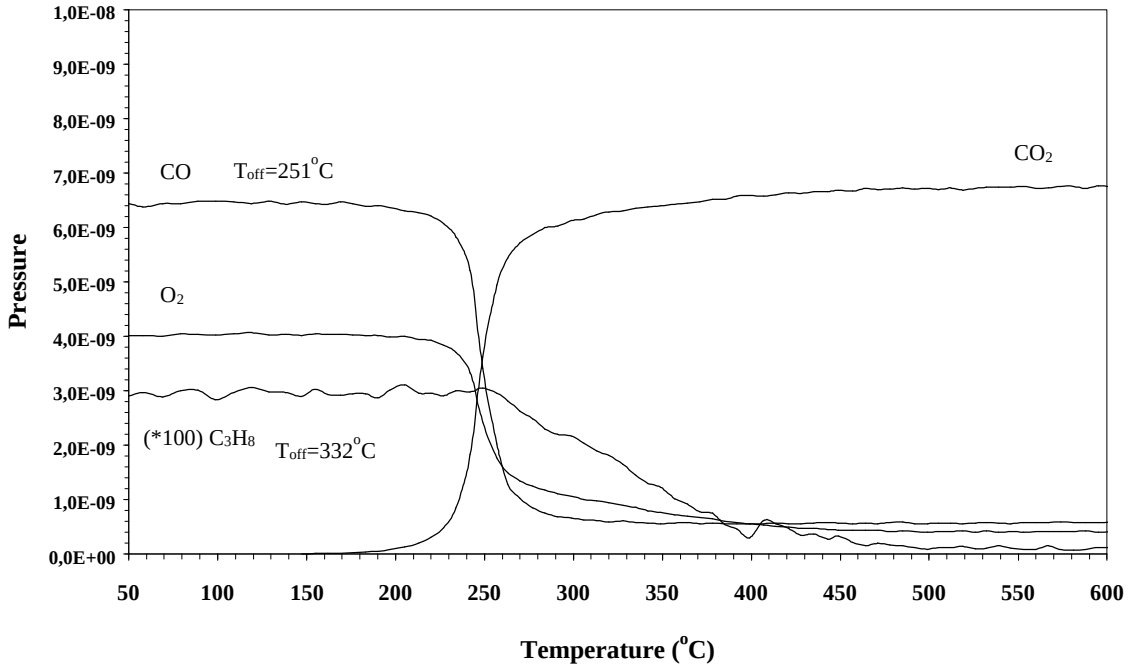


Fig. 29. Conversion of CO and $C_3H_6$ on spinel catalysts, the light off temperature was 251°C for CO and 332°C for $C_3H_6$ combustion.

## 5.5 Magnetic Properties of Iron Oxide Materials

The electron diffraction technique was used to analyze the crystal structure of the iron oxide samples. The diffraction pattern did not seem to depend much on the oxygen pressure in the chamber during the synthesis. Similar structures were obtained for all samples and also for particles of all sizes. It is difficult to see the difference between $Fe_3O_4$ and $\gamma$-$Fe_2O_3$ in the diffraction pattern because these structures are isomorphic and lines are located very close to each other. The color of the samples changed from very dark brown to reddish-brown with increasing oxygen pressure which means that a change from $Fe_3O_4$ to $\gamma$-$Fe_2O_3$ structure. No $\alpha$-$Fe_2O_3$ structure was seen in the samples.

To further analyze the chemical composition of the iron oxides infrared spectroscopy was used. Broad peaks typical to a quasi-amorphous phase [97] were seen in IR analysis (Fig. 30). As the partial oxygen pressure increased the peaks due to $\gamma$-$Fe_2O_3$ (two peaks at 570 and 450 $cm^{-1}$ [97]) increased and the $Fe_3O_4$ peak (one peak at 580 $cm^{-1}$ [97]) decreased. Samples prepared in pure helium gas and in absence of oxygen were dominated by $Fe_3O_4$ spectrum with some $\gamma$-$Fe_2O_3$ present. The addition of oxygen (10 or 500 Torr) changed the IR spectrum indicating that $\gamma$-$Fe_2O_3$ became the major phase.

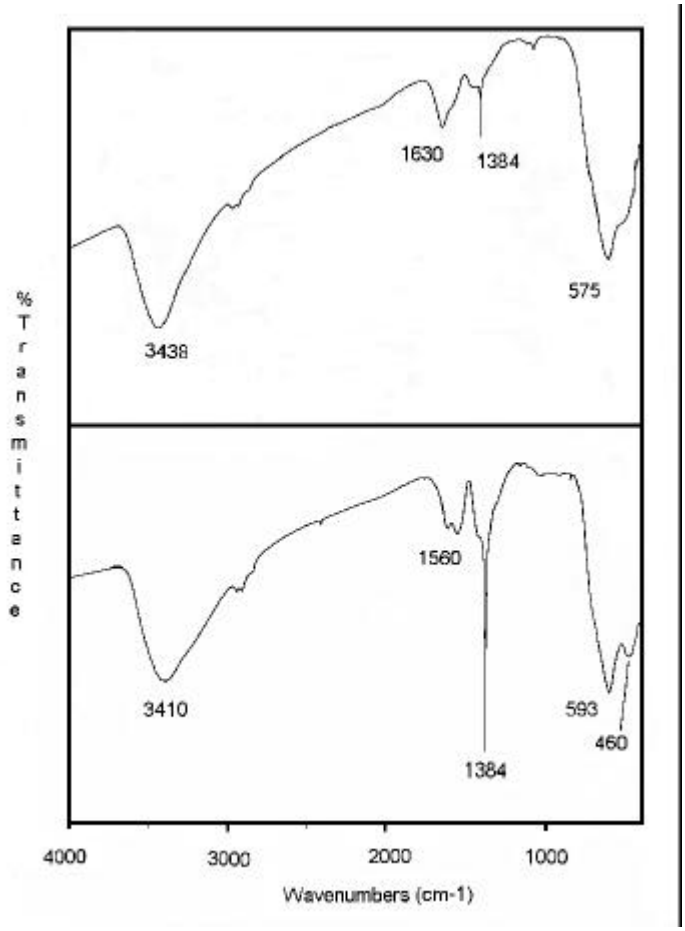


Fig. 30 Infrared spectra of the iron oxide samples prepared in helium atmosphere (top) and at 500 torr oxygen (bottom).

IR spectra of the sample prepared in pure nitrogen atmosphere showed the formation of $Fe_3O_4$ phase and a peak at 2058 $cm^{-1}$ due to an azide group. The FTIR technique is suitable for surface species analysis. Peaks due to the surface adsorbed hydrocarbons ($CH_2$ vibrations at 2930-2970 $cm^{-1}$), $CO_2$ ($CO_3^{2-}$ peaks at 1420, 1384 and 878 $cm^{-1}$) and water (3000-3700, and 1630 $cm^{-1}$) can be seen.

The magnetic properties of prepared iron oxide particles were analyzed in terms of superparamagnetism. In the particle size analysis a few very large particles (up to 500 nm) were seen and that does have an affect on the results. On the baseline of the superparamagnetic behavior the magnetization of the ferromagnetic oxide particles can be seen which have coercivity even at room temperature. The temperature dependence of the

magnetization of these iron oxide particles show superparamagnetic behavior with varying blocking temperatures as a result of using different partial oxygen pressures.

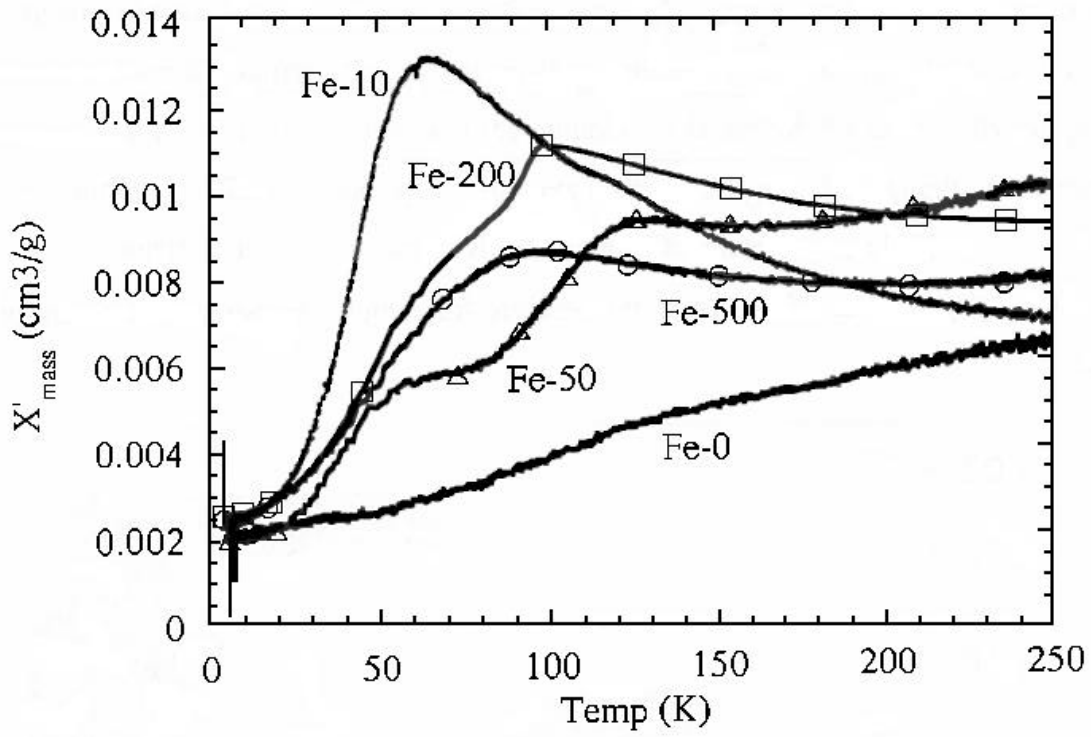


Fig. 31. In-phase AC susceptibility of iron oxide samples as a function of time.

The particle size was determined from the magnetic measurements and found to be 6 nm. It was in good agreement with the particle size obtained from TEM micrographs. The coercivity of superparamagnetic particles showed clear temperature dependence as expected. Also the frequency dependence of the blocking temperature was typical for superparamagnetic samples.

## 6. CONCLUSIONS AND FUTURE WORK

Laser vaporization- controlled condensation has been shown to be a very useful technique for the preparation of nanophase metal oxides and carbides. The temperature gradient and the selection of inert gas control both the size and the crystal structure of particles. The degree of oxidation of metals can be controlled by the reactant / inert gas ratio. The surface analysis of laser vaporized samples show very clean surfaces with low carbon contamination and increased redox reactivity due to surface hydroxyl groups. The formation of new molybdenum carbide materials in macroscopic amounts was discovered and the formation of fullerenes and polymerization were observed as by-products. The magnetic properties of iron oxide particles changing from ferromagnetic to superparamagnetic is an example of the size effects of nanoparticles.

Coprecipitation can be used to prepare of multi-component solid solution oxides. The constitution of organometallic precursors during synthesis was studied and the agglomeration was found to be due to the diffusion controlled cluster-cluster collision mechanism. The effect of different synthesis conditions on the size of the particles can be predicted using DLVO- theory. Ostwald ripening changes the particle morphology drastically during the synthesis and after two hours of mixing micrometer-size particles were observed. The effect of the precipitation procedure on the catalytic activity of doped ceria was found to be negligible.

The origin of catalytic activity of cerium oxide based catalysts was investigated and the electronegativity of the dopant was found to be of importance. It affects the growth of particle size of the oxide and the light-off temperature of carbon monoxide on the oxide catalyst. The oxidation of propene was found to depend on the heat of formation of the oxide that is related to the heat of adsorption. The activity of the noble metal loaded ceria catalyst was found to be dependent on the acidity of the oxide phase.

### Outlook for future work

On the preparation side development of new methods, which can in an inexpensive way produce materials with small particle size, narrow size distribution and weak agglomeration and necking on a large scale is sought. This would create new possibilities for functional multicomponent materials.

To be useful as an optoelectronic material, porous silicon must provide bright electroluminescence, not photoluminescence, at useful wavelengths and with reasonable quantum efficiencies. Generally the EL reported so far is weak compared to the bright PL. One potential application of porous silicon is to drive fiber-optic optical systems, which would require bright and very fast EL. Another potential application is in EL displays, which would not require high speed, but a very bright, visible EL source. To determine the optimum material’s solid state structure for producing EL for a particular application, the physical mechanisms responsible for the EL and for the carrier transport must be well understood.

Nanoparticles showing superparamagnetism can not be used in magnetic recording. Materials with high blocking temperature enable a decrease in grain size which is required for

recording media. Chemical stability is also important in this application and a method to avoid the oxidation of metallic materials is anticipated.

It would be interesting to continue the work with doping of ceria and optimize the composition. It would be important to gain a deeper understanding about the activity in order to be able to predict the activity of the material as well as its surface area. The fundamental understanding of catalytic reactions under operating conditions is generally poorly understood and this field offers numerous possibilities for future work.

## 7. ACKNOWLEDGEMENTS

There are so many people I want to thank. These years in graduate school have been the best years of my life. I have had the privilege to work in four different research groups, to visit several different countries and have met people from all over the world representing many cultures. The best of all I have made lot of new friends and learned to appreciate what I have. I never take anything for granted but I know that I can make a difference by trying. I think that I have become a better person during these years accepting different opinions and not judging people because of their opinions. It has been a great experience.

First and foremost I want to thank my supervisor, Prof. Mamoun Muhammed for giving me the opportunity to be involved in this interesting field of materials science.

I also want to thank the other professors who have given me guidance during these years, namely Prof. K.V. Rao at Royal Institute of Technology and Prof. M. Samy El-Shall at the Virginia Commonwealth University.

Many thanks to the people I have worked with. The collaboration with Dr. Michel Trudeau, Dr. Lothar Mussmann and Dr. Stephane Romero is greatly appreciated.

I thank all the people in the groups in which I have worked with and all my friends as well. You are too many to be mentioned here but you have made my life enjoyable both at work and in my free time.

Finally I want to thank Neste OY's foundation for their financial support. It made it possible for me to study and learn so much during these years. The financial support from KTH grant for internationalization of graduate students and the Franz Georg and Gull Liljenroth foundation made it possible for me to visit the University of California, Berkeley. Part of the research was financed by the TFR and Brite Euram program BRPR-CT96-0290.

I owe so much to my lovely family who have been so supportive.

Thank you all.

## 8. REFERENCES


1. Siegel, R.W., *Physics of New Materials* (Ed. Fujita, F.E.), Springer-Verlag Berlin Heidelberg, Chapter 4, (1994).
2. Somorjai, G.A., *Pure & Appl. Chem*. **50**, 963-969 (1978).
3. Andres, R.P., Averback, R.S., Brown, W.L., Brus, L.E., Goddard, III, W.A., Kaldor, A., Louie, S.G., Moscovits, M., Peercy, P.S., Riley, S.J., Siegel, R.W., Spaepen, F., and Wang, Y., *J. Mater. Res*. **4**, 704-736 (1989).
4. Gleiter, H., *Z. Metallkd*. **86**, 78-83 (1995).
5. Klabunde, K.J., Li, Y-X. and Khaleel, A., *Nanophase Materials* (Eds. Hadjipanayis, G.C. and Siegel, R.W.) Kluwer Academic Publishers, the Netherlands 757-769 (1994).
6. Somorjai, G.A., *Surface Chemistry and Catalysis*, John Wiley & Sons, Inc., New York, 1994.
7. Tanabe, K., Sumiyoshi, T., Shibata; K., Keyoura, T. and Kitagawa, J., *Bull. Chem. Soc. Jpn* **47**, 1064-1066 (1974).
8. Liu, Z., Tabora, J., and Davis, R.J., *J. Catal*. **149**, 117-126 (1994).
9. Kung, H.H., *Transition metal oxides: Surface Chemistry and Catalysis*, Elsevier, Amsterdam, 43-91 (1989).
10. Wojciechowski, B.W., *Catalytic Cracking: Catalysts, Chemistry, and Kinetics*, Dekker, New York, (1986).
11. Somorjai, G., *New J. Chem*. **11**, 197-200, (1987).
12. Papp, J., Soled, S., Dwight, K., and Wold, A., *Chem Mater*. **6**, 496-500 (1994).
13. Wold, A., *Chem Mater*. **5**, 280-283 (1993).
14. Kreuzer, T., Lox, E.S., Lindner, D., and Leyer, J., *Catal. Today*, **29**, 17-27 (1996).
15. Kiselev, V.F. and Krylov, O.V., *Adsorption and Catalysis on Transition Metals and Their Oxides*, Springer-Verlag, Berlin, (1989).
16. Bunluesin, T., Cordatos, H., and Gorte, R.J., *J. Catal*. **157**, 222-226 (1995).
17. Niemantsverdriet, J.W., *Appl. Phys*. **A 61**, 503-509 (1995).
18. Dubois, L.H., Hansma, P.K., and Somorjai, G.A., *J. Catal*. **65**, 318-327 (1980).
19. Van Hardeveld, R.M., Schmidt, A.J.G.W., and Niemantsverdriet, J.W., *Catal. Lett*. **41**, 125-131 (1996).
20. Tschöpe, A., and Ying, J.Y., *Nanophase Materials* (Eds. Hadjipanayis, G.C. and Siegel, R.W.) Kluwer Academic Publishers, the Netherlands 781-784 (1994).
21. Ying, J.Y., *Nanophase Materials* (Eds. Hadjipanayis, G.C. and Siegel, R.W.) Kluwer Academic Publishers, the Netherlands, 197-204 (1994).
22. Conner, W.C., Jr, and Falconer, J.L., *Chem. Rev*. **95**, 759-788 (1995).
23. Vaarkamp, M., Miller, J.T., Modica, F.S., Koningsberger, D.C., *J. Catal*. **163**, 294-305 (1996).
24. Giannelis, E.P., Mehtora, V., Vassiliou, J.K., Shull, R.D., MacMichael, R.D., and Ziolo, R.F., *Nanophase Materials* (Eds. Hadjipanayis, G.C. and Siegel, R.W.) Kluwer Academic Publishers, the Netherlands 197-204 (1994).
25. Brus, L., *J. Phys. Chem*. **98**, 3575-3581 (1994).
26. Kittel, C., *Introduction to Solid State Physics*, John Wiley and Sons, Inc., (1992), pp. 183-187.
27. Wilson, W.L., Szajowski, P.F., and Brus, L.E., *Science* **262**, 1242-1244 (1993).
28. Brus, L.E., *Nanophase Materials* (Eds. Hadjipanayis, G.C. and Siegel, R.W.) Kluwer Academic Publishers, the Netherlands 433-448 (1994).
29. Canham, L.T., *Appl. Phys. Lett*. **57**, 1046 (1990).

30. Hamilton, B. and Gardelis, S., *Optical Properties of Low Dimensional Silicon Structures* (Eds. D.C. Bensahel et al.) Kluwer Academic Publishers, the Netherlands 35-41 (1993).
31. Takazawa, A., Tamura, T., and Yamada, M., *J. Appl. Phys.* **75**, 2489-2495 (1994).
32. Bois, D. and Debever, J.M.,*Optical Properties of Low Dimensional Silicon Structures* (Eds. D.C. Bensahel et al.) Kluwer Academic Publishers, the Netherlands 169-178 (1993).
33. Pavesi, L., Calliari, L., Zanghellini, E., Mariotto, G., Anderle, M. and Bisi, O., *Optical Properties of Low Dimensional Silicon Structures* (Eds. D.C. Bensahel et al.) Kluwer Academic Publishers, the Netherlands 61-67 (1993).
34. Dubin, V.M., Ozonam, F. and Chazalviel, J.-N., *Optical Properties of Low Dimensional Silicon Structures* (Eds. D.C. Bensahel et al.) Kluwer Academic Publishers, the Netherlands 211-217 (1993).
35. Nozaki, S., Sato, S., Ono, H. and Morisaki, H., *Mat. Res. Soc. Symp. Proc*. **351**, 399-404 (1994).
36. Harvey, J.F., Poindexter, E.H., Morton, D.C., Rong, F.C., Lux, R.A., and Tsu, R., *Optical Properties of Low Dimensional Silicon Structures* (Eds. D.C. Bensahel et al.) Kluwer Academic Publishers, the Netherlands 179-190 (1993).
37. Bsiesy, A., Muller, F., Ligeon, M., Gaspard, F., Herino, R., Romestain, R. and Vial, J.C., *Phys. Rev. Lett*. **71**, 637-640 (1993).
38. Kozlowski, F., Steiner, P. and Lang, W., *Optical Properties of Low Dimensional Silicon Structures* (Eds. D.C. Bensahel et al.) Kluwer Academic Publishers, the Netherlands 123-132 (1993).
39. Skuja, L.N.,Streletsky, A.N. and Pakovich;A.B., *Solid State Comm*. **50**, 1069-1072 (1984).
40. Morisaki, H., Hashimoto, H., Ping, F.W., Nazawa, H. and Ono, H., *J. Appl. Phys*. **74**, 2977-2979 (1993).
41. Guzzi, M., Martini, M., Mattaini, M., Pio, F. and Spinolo, G., *Phys Rev. B* **35**, 9407-9409 (1987).
42. Ashcroft, N.W., Mermin, N.D., *Solid State Physics*, Saunders Collage Publishing, 718-722 (1976).
43. Wohlfarth, E.P., *Ferromagnetic Materials vol 2*., North-Holland Publishing Company, Amsterdam, 436-444 (1980).
44. Mallinson, J.C., *The Foundations of Magnetic Recording*, Academic Press, San Diego, USA, 28-30 (1987).
45. Cullity, *Introduction to Magnetic Materials*, Addison Wesley Publishing Company, Reading, USA, 410-418 (1972).
46. Gangopadhyay, S., Hadjipanayis, G.C., Sorensen, C.M. and Klabunde, K.J., *Mater. Res. Soc. Sym. Proc*. **286**, 55-60 (1993).
47. Gangopadhyay, S., Hadjipanayis, G.C., Dale, B., Sorensen, C.M., Klabunde, K.J., Papaefthymiou, V. and Kostikas, A., *Phys. Rev. B.* **45**, 9778-9787 (1992).
48. Uchikoshi, T., Sakka, Y., Yoshitake, M., and Yoshihara, K., *Nanostructured Mater*. **4**, 199-206 (1994).
49. Yiping, L., Hadjipanayis, G.C., Papaefthymiou, V., Soerensen, C.M., and Klabunde, K.J., *Nanophase Materials* (Eds. Hadjipanayis, G.C. and Siegel, R.W.) Kluwer Academic Publishers, the Netherlands 625-633 (1994).
50. Dormann, J.L., Fiorani, D. and Tronc, E., *Nanophase Materials* (Eds. Hadjipanayis, G.C. and Siegel, R.W.) Kluwer Academic Publishers, the Netherlands 635-644 (1994).
51. Siegel, R.W. and Fougere, G.E., *Mater. Res. Soc. Sym. Proc*. **362**, 219-229 (1995).

52. Siegel, R.W. and Fougere, G.E., *Nanophase Materials* (Eds. Hadjipanayis, G.C. and Siegel, R.W.) Kluwer Academic Publishers, the Netherlands, 233-261 (1994).
53. Siegel, R.W. and Fougere, G.E., *Mater. Res. Soc. Sym. Proc*. **286** 219-229 (1994).
54. Gutmanas, E.Y., Trusov, L.I., and Gotman, I., *Nanostructured Mater*. **4**, 893-901 (1994).
55. McCandlish, L.E., Kear, B.H. and Kim, B.K., *Nanostructured Mater*. **1**, 119-124 (1992).
56. Gleiter, H., *Nanostructured Mater*. **1**, 1-19 (1992).
57. Udaphyaya, G.S., *Cemented Tungsten Carbides; Production, Properties, and Testing*, Noyes Publications, Westwood, USA, (1998).
58. Goodenough, J.B., Manthiram, A., Paranthaman, M, and Zhen, Y.S., *Solid State Ionics*, (Eds. Balanski, M., et al.), Elsevier, Amsterdam, 79-90 (1992).
59. Etsell, T.H., and Flengas, *Chem. Rev.* **70**, 339-376, (1970).
60. Ashcroft, N.W., Mermin, N.D., *Solid State Physics*, Saunders Collage Publishing, 2-11, 616-623 (1976).
61. Chiang, Y.-M., Mass and Charge Transport in Ceramics, 79-89.
62. Chiang, Y.-M., Lavik, E.B., Kosacki, I., Tuller, H.L., and Ying, J.Y., J. Electroceramics **1**, 7-14 (1997).
63. Chiang, Y.-M., Lavik, E.B., Blom, D.A., *Nanostr. Mat*. **9**, 633-642 (1997).
64. Granqvist, C.G. and Buhrman, R.A., *J. Appl. Phys*. **47**, 2200-2219 (1976).
65. El-Shall, M.S., Slack, W., Vann, W., Kane, D. and Hanley, D., *J. Phys. Chem*. **98**, 3067 - 3070 (1994).
66. El-Shall, M.S., Slack, W., Vann, W.,Hanley, D. and Kane, D., *Mat. Res. Soc. Symp. Proc.* **351**, 369-374 (1994).
67. Gaertner, G.F., and Lydtin, H., *Nanostruct. Mater.* **4**, 559-568 (1994).
68. Luce, M., Herlin, N., Musset, E., and Cauchetier, M., *Nanostruct. Mater.* **4**, 403-408 (1994).
69. Zhao, X.Q., Liang, Y., Cui, Z.J., Xiao, K., Zheng, F. and Hu, Z.Q., *Nanostructur. Mater.* **4**, 397-402 (1994).
70. Herlin, N., Croix, O., Luce, M., Cauchetier, M., Legrand, A.P., Hommel, H. and Tougne, P., *Nanophase Materials* (Eds. Hadjipanayis, G.C. and Siegel, R.W.) Kluwer Academic Publishers, the Netherlands 93-96 (1994).
71. Flagan, R. and Lunden, M., *Mat. Sci. & Eng*. **A204**, 113-24 (1995).
72. Edelstein, A.S., *Nanophase Materials* (Eds. Hadjipanayis, G.C. and Siegel, R.W.) Kluwer Academic Publishers, the Netherlands, 73-80 (1994).
73. Ring, T., *Ceramic Powder Processing*, Academic Press, USA, Chapter 6 (1996).
74. Greenwood, N.N., and Earnshaw, A., *Chemistry of the Elements*, Pergamon Press, Great Britain, (1984).
75. Mallinson J.C., *The Foundations of Magnetic Recording*, Academic Press, Inc, San Diego, USA, 28-30 (1987).
76. Kroto, H.W., Heath, J.R., O´Brien, S.C., Curl, R.F. and Smalley, R.E., *Nature* **318**, 162-163 (1985).
77. Krätschmer, W., Lamb, L.D., Fostiropoulos, K. and Huffman, D.R., *Nature* **347**, 354-358 (1990).
78. Zhang, B.L., Wang, C.Z. and Ho, K.M., *Chem Phys. Lett*. **193**, 225-230 (1992).
79. Sunderlin, L.S., Paulino, J.A., Chow, J., Kahr, B., Ben-Amotz, D. and Squires, R.R., *J. Am. Chem. Soc.* **113**, 5489-5490 (1991).
80. Saxby. Saxby, J.D., Chatfield, S.P., Palmisano, A.J., Vassallo, A.M., Wilson, M.A. and Pang, L.S.K., *J. Phys. Chem*. **96**, 17-18 (1992).

81. Taylor, R., Hare, J.P., Abdul-Sada, A.K. and Kroto, H.W., *Chem. Commun*., 1423-1425 (1990).
82. Taylor, R. and Walton, D.R.M., *Nature* **363**, 685-693 (1993).
83. Chai, Y., Guo, T., Jin, C., Haufler, R.E., Chibante, L.P.F., Fure, J., Wang, L., Alford, J.M., and Smalley, R.E., *J. Phys. Chem*. **95**, 7564-7568 (1991).
84. Shinohara, H., Sato, H., Ohkohchi, M., Ando, Y., Kodoma, T., Shida, T., Kato, T. and Saito, Y., *Nature* **357**, 52-54 (1992).
85. Guo, T., Diener, M.D., Chai, Y., Alford, M.J., Haufler, R.E., McClure, S.M., Ohno, T., Weaver, J.H., Scuseria, G.E. and Smalley, R.E., *Science* **257**, 1661-1664 (1992).
86. Fleming, R.M., *Proceedings of the Joint Nordic Spring Meeting '92*, Roskilde, Denmark 33-34 (1992).
87. Chen, C.-C. and Lieber, C.M., *J. Am. Chem. Soc.* **114**, 3141-3142 (1992).
88. Guo, B.C., Kerns, K.P. and Castleman, A.W.,Jr., *Science* **255**,1411-1413 (1992).
89. Guo, B.C.,Wei,S., Purnell, J., Buzza, S., and Castleman, A.W.,Jr., *Science* **256**, 515-516 (1992).
90. Wei, S., Guo, B.C., Purnell, J., Buzza, S., and Castleman, A.W.,Jr., *Science* **256**, 818-820 (1992).
91. Jin, C., Haufler, R.E., Hettich, R.L., Barshick, C.M., Compton, R.N., Puretzky, A.A., Dem′yanenko,A.V. and Tuinman, A.A., *Science* **263**, 68-71 (1994).
92. Wright, D., Caldwell, R., Moxely, C., El-Shall, M.S., *J. Chem. Phys*. **98**, 3356 (1993).
93. Weisshaar, J.C., *Laser Chemistry of Organometallics*, (Ed. Chaiken, J.), *ACS Symp. Series*, **530**, 208-219 (1993).
94. Fessenden, R.J., Fessenden, J.S., *Organic Chemistry, 3rd Edit.*, Brooks/Cole Publishing Company, Monterey, (1986).
95. Fievet, F., Lagier, J.P., Figlarz, M., *MRS Bulletin*, 29-34 (Dec. 1989).
96. Trudeau, M.L., Tschöpe, A. and Ying, J.Y., *Surface and Interface Analysis* **23**, 219-226 (1995).
97. Baraton, M.I., Unpublished results.